water

MDPI

Article

An Integrated GIS and Remote Sensing Approach for Assessing Rainfall Volume and Groundwater Recharge in Wadi AS SAHBAA, Saudi Arabia

Hany Mohamed [1], Motrih Al-Mutiry [2], Emad Hafez [1], Ali Al-Balushi [3], Hussein Almohamad [4], Ali Shebl [5,6,*] and Mohamed A. Atalla [7,8,*]

[1] Department of Geography and GIS, Faculty of Arts, Beni-Suef University, Beni Suef 62511, Egypt; hany.mohamed@art.bsu.edu.eg (H.M.); emad.hafez@art.bsu.edu.eg (E.H.)
[2] Department of Geography and Environmental Sustainability, College of Humanities and Social Sciences, Princess Nourah bint Abdulrahman University, P.O. Box 84428, Riyadh 11671, Saudi Arabia; mkalmutairy@pnu.edu.sa
[3] Department of Geography, College of Arts and Social Sciences, Sultan Qaboos University, P.O. Box 79, Muscat City 123, Oman; buloshis@squ.edu.om
[4] Department of Geography, College of Languages and Human Sciences, Qassim University, Buraydah 51452, Saudi Arabia; h.almohamad@qu.edu.sa
[5] Department of Geology, Tanta University, Tanta 31527, Egypt
[6] Department of Mineralogy and Geology, University of Debrecen, 4032 Debrecen, Hungary
[7] Department of Natural Studies, General Organization for Physical Planning (GOPP), Ministries District, New Administrative Capital, Cairo 85863, Egypt
[8] Department of GIS and Environment, Enshaat Al-Sayer General Trading and Contracting Company, Floors 14 & 19, Panasonic Tower, Safat, P.O. Box 126, Kuwait City 13002, Kuwait
* Correspondence: ali.shebl@science.tanta.edu.eg (A.S.); atallahm763@gmail.com (M.A.A.)

Abstract

Water security is a significant challenge for the Saudi Arabia Kingdom's development and stability, affecting other economic sectors beyond the water sector. Insufficient water resources are causing economic and social crises; addressing this issue is crucial for the country's growth and stability. This study aims to manage water resources in central Saudi Arabia (Wadi AS SAHBAA) through a two-level approach. The first level involves extracting rainfall amounts from satellite imagery to predict future rainfall intensity using PERSIANN-CCS-CDR data. The second level focuses on monitoring groundwater recharge using geographic information systems (GIS) and remote sensing techniques. The study further seeks to understand rainstorm behavior influenced by climate variability and applies geomatics techniques for quantitative analysis. The results show that the Wadi AS SAHBAA basin receives an annual precipitation of 116.6 mm/year and mean annual precipitation of 9.7 mm. The year 2019 experienced the highest recorded precipitation, reaching 222.3 mm and mean annual precipitation of 18.5 mm. Between 2013 and 2019, the AS SAHBAA region experienced increased rainfall driven by intense storm events; however, it declined during the period 2020–2022. Moreover, 2021 recorded the lowest annual precipitation of 53.8 mm with mean annual precipitation of (4.5 mm), possibly linked to reduced storm activity due to the COVID-19 pandemic. The study uses several methods to estimate groundwater recharge from rainfall and concludes that the average infiltration during 2013–2022 was varying from 1.59–36.63 mm, representing about between 1.03 and 28.5% of total rainfall. This is reflected in groundwater storage capacity, which ranges from approximately 1.65 to 38.27 million m^3 yearly. This study provides a framework for monitoring precipitation and groundwater recharge and offers practical recommendations for regional development and sustainable water management.

Check for updates

Academic Editors: Athanasios Loukas and Cesar Andrade

Received: 12 May 2026
Revised: 3 August 2026
Accepted: 7 August 2026
Published: 18 August 2026

Copyright: © 2026 by the authors. Licensee MDPI, Basel, Switzerland. This article is an open access article distributed under the terms and conditions of the Creative Commons Attribution (CC BY) license.

Keywords: water management strategy; freshwater resources; rainfall intensity; PERSIANN-CCS-CDR; groundwater recharge; geomatics techniques; infiltration; storage capacity

1. Introduction

World countries, especially dryland countries, face significant challenges in managing water resources due to the rapid increase in urban and rural populations, coupled with surface water scarcity in dry seasons, climate change, urbanization, deforestation, land degradation, and expanded irrigation systems, which has heightened concerns regarding the sustainable management of water resources [1–5]. Water is crucial for economic and social development, meeting human needs, managing environmental issues, and ensuring economic sustainability [6–8]. The management of water resources, including rivers, groundwater, and catchments, is crucial for environmental, economic, and political reasons [9]. Climate change increases the frequency of disasters and environmental consequences, but hydrological factors like slope, vegetation, elevation, and urbanization contribute to flash floods. However, hydrological measurements and observations are sporadic and insufficient to fully understand hydrological processes [10,11]. Most data are limited and gathered through pilot projects and independent case studies, which cannot represent the diversity within dryland settings [12]. The interaction between surface water and groundwater is crucial for understanding the quantitative and qualitative regime of dependent hydrosystems [13]. A multi-scale approach combining cross-disciplinary techniques can reduce uncertainties and provide an optimal understanding of groundwater and surface water exchanges. The simulation process is an effective tool for this analysis but requires a variety of data, detailed hydrosystem analysis, and time to finalize a reliable solution. The results of the simulation process contribute to raising awareness for water protection and improving management strategies.

Climate change, characterized by high temperatures, precipitation, floods, and global sea-level rise, is the most significant issue in recent decades [14,15]. Globally, severe weather conditions are prevalent, leading to flooding and significant infrastructure damage [16,17]. A long-term, accurate precipitation dataset is necessary for analyzing climate simulation models and hydrological studies [18–22]. Precipitation is a crucial component of the global hydrological cycle and plays a vital role in regulating the climate system [23–25]. Precipitation estimation is crucial for essential phenomena like ground-water recharge assessment and flood and drought monitoring, highlighting its importance in water resources [26–29]. Precipitation estimates are typically conducted using on-ground rain gauges, which provide real-time rainfall data but lack geographically dispersed data [30–32]. Long-term data gauge monitoring systems require significant financial and technological investment.

Rainfall quantification is challenging due to unequal distribution and geographical inhomogeneity, especially in dry and semi-arid environments with strong rainfall intensity. Spatial unevenness in storms further complicates the process [33–39]. During the last three decades, numerous satellite-based global precipitation datasets have been developed and implemented, with spatial resolutions ranging from 0.04° to 2.5°, temporal resolutions from 30 min to monthly intervals, and temporal coverage extending up to 40 years. Their usability depends on the application type, accuracy, latency, and temporal and spatial resolutions of the estimates [40–42]. The spatial and temporal variability of precipitation strongly affects catchment behavior and the performance of hydrological models. Therefore, high-resolution precipitation datasets are essential for accurately simulating runoff processes [43–49]. The Tropical Rainfall Measurement Mission (TRMM) in 1997 advanced

satellite-based precipitation products. The 2018 GPM mission, launched with multiple passive microwave sensors, provides global coverage through combined observations [50–55]. PERSIANN-CCS-CDR is a satellite-derived precipitation product that provides daily rainfall estimates spanning more than 30 years at a spatial resolution of 0.25° × 0.25° across the 60°S–60°N latitudinal range [56]. The PERSIANN-CDR algorithm uses GridSat-B1's infrared brightness temperature archive as input and then uses the monthly Global Precipitation Climatology Project (GPCP) version 2.3 product to bias-correct rainfall estimates at 2.5° × 2.5° spatial resolution [57–59]. PERSIANN-CCS is a cloud-patch algorithm that extracts features from infrared cloud images under specific temperature thresholds, including segmentation, extraction of temperature, geometry, texture, classification using SOFM clustering algorithm, and relationship between brightness temperature and rainfall rate [60]. The 2014 NASA GPM IMERG algorithm, a PMW rainfall calibrated PERSIANN-CCS, is now available for public use through the CHRS data portal [50,61].

Groundwater recharge is crucial for sustainable groundwater development, and quantification of recharge amounts in groundwater aquifers is essential for sustainable development [62–65]. Groundwater recharge may occur naturally through direct infiltration of precipitation or seepage from adjacent water bodies, as well as artificially through human activities such as irrigation, urban development, and river diversion. Not all rainwater reaching the ground infiltrates or contributes to groundwater recharge, as portions are lost through evaporation, transpiration, and surface runoff. The infiltrated fraction replenishes soil moisture and recharges the aquifer [66]. Baseflow separation is the most used technique for estimating groundwater discharge and recharge from streamflow records. This method involves estimating a continuous record of baseflow from the hydrograph, requiring long-term records and manual methods [67–71]. The link between the expansion of irrigated agricultural land and groundwater depletion was very important, as irrigated areas grew and groundwater levels fell, demonstrating a reliance on groundwater due to a lack of surface-water sources [72].

The Arabian Peninsula is facing severe water scarcity due to population growth, urbanization, and climate change. The region's arid and semi-arid climates rely on groundwater resources for freshwater, but groundwater depletion is a major concern [73]. The region's arid to semi-arid climate is causing extreme stress to groundwater resources due to high temperatures, low rainfall, and high evapotranspiration [74,75]. The kingdom of Saudi Arabia (KSA) is grappling with significant challenges due to high agricultural demand and the elevated costs associated with water supply and drainage services in urban areas [76,77]. During the 1970s, groundwater resources were primarily used for agriculture, but rapid urbanization, industrial growth, and population growth have led to a growing concern for the quantity and quality of groundwater resources in water-stressed regions [78]. KSA ranks third globally in freshwater consumption, increasing from 227 L/capita/day in 2009 to 278 L/c/day in 2018; however, 80% of the country's water supply demand come from groundwater [79,80]. Over the past three decades, groundwater exploitation in KSA has significantly increased, reaching 17 billion m^3/year [81]. Future irrigation water demands are expected to increase as a result of projected temperature rises in regions such as Al Quassim, Al Jawf, Ha'il, Al Madinah, the Northern region, Najran, Baha, and Tabuk, leading to a greater need for water resources [49]. The kingdom's water requirements, estimated at 24.8 billion cubic meters in 2015, are increasing at a constant 7% rate, with the agricultural sector accounting for 84% of the total water demand [82]. The demand–supply imbalance, worsened by climate change, has led to the rapid depletion of nonrenewable groundwater reserves, rendering water a scarce renewable resource in arid climates [83–85].

Despite the considerable number of studies addressing groundwater resources and precipitation estimation in arid and semi-arid regions, several critical research gaps still

exist. First, most previous studies in the Arabian Peninsula, particularly in the kingdom of Saudi Arabia, have primarily relied on either ground-based observations or single-source satellite datasets, with limited efforts to integrate long-term, high-resolution satellite precipitation products such as PERSIANN-CCS-CDR with hydrological and groundwater recharge assessments. Second, there is a lack of comprehensive spatio-temporal analysis linking climate variability, precipitation dynamics, and groundwater recharge processes under changing climatic conditions, especially at regional and basin scales. Moreover, previous research has often focused on either groundwater depletion or precipitation variability independently, without establishing a robust quantitative relationship between rainfall patterns and groundwater recharge coefficients. In addition, the uncertainties associated with satellite-based precipitation estimates in arid environments—characterized by high spatial variability and extreme rainfall events—remain insufficiently evaluated. Therefore, this study introduces a novel integrated approach that combines long-term satellite-derived precipitation datasets (PERSIANN-CCS-CDR) with groundwater recharge estimation techniques to assess the spatio-temporal variability of recharge processes in a data-scarce arid environment. The study further enhances existing methodologies by incorporating recharge coefficient analysis and evaluating the reliability of satellite precipitation data for hydrological applications in Saudi Arabia. This integrated framework provides new insights into sustainable groundwater management under climate change and supports decision-makers in optimizing water resource utilization in arid regions.

2. Materials and Methods

2.1. Study Area

Wadi AS SAHBAA is one of the largest drainage basins in the kingdom of Saudi Arabia, extending across the central part of the country along a southwest–northeast axis. The basin originates in the highlands of central Saudi Arabia, particularly within the Tuwaiq Mountains, and terminates at Sabkhat Al-Hamr, located in the Eastern Province near the Al-Batha border crossing. After traversing the Ad-Dahna Desert, the wadi re-emerges approximately 100 km further east under a different local name. Historical cartographic records dating from the 12th to the 19th centuries depict this drainage system as a continuous linear feature extending across the Arabian Peninsula, commonly referred to as Wadi Afnan [86,87]. The valley's upper basin comprises two ancient river systems from the Pleistocene and Holocene eras: Wadi Lahi in the south and Wadi Barak in the north, which meet in the Al-Kharj region after crossing the Tuwaiq Mountains [88]. Spatially, Wadi AS SAHBAA extends between latitudes 21°35′14.368″ and 25°26′12.695″ N and longitudes 42°50′30.443″ and 51°06′49.466″ E (Figure 1). The total area of the basin is approximately 138,677.3 km^2, encompassing 126 sub-basins that range in size from 18.6 to 24,473.1 km^2. The basin is bordered by several major urban centers, including Riyadh, Al-Kharj, and Hawtat Bani Tamim. Overall, the wadi extends for approximately 845 km along a west–east axis, with its headwaters located in the elevated terrains of central Saudi Arabia.

The study area's geographical location in the central part of the Arabian Peninsula, combining highlands, plains, and valley courses, contributed to its diverse geological features. This exposure of various layers influenced the region's geomorphology and the rate of surface water feeding the groundwater reservoir. The Wadi AS SAHBAA, covering 7.2% of Saudi Arabia's kingdom, is part of the Najd Plateau, where limestone rocks whose formation dates to the Jurassic and Cretaceous periods in the second era and to the Eocene and Miocene periods in the third era [89,90]. With a total length of 208,747 km, the Wadi AS SAHBAA Basin is made up of 126 sub-basins and 117,825 streams. With 18.6% of the valley's total area, the Barak Valley is the biggest tributary. The Lahi Valley comes in second with 10.5%. Its tributaries include Wadi Al-Khumrah, Al-Amariyah, Bir Namar,

Shuaib Laha, Baija, and Wadi Al-Ist and Al-Batha'. The city of Riyadh is situated on Wadi Al-Batha', with its confluence with Wadi Hanifa. The valley is home to numerous villages and towns, including Al-Ainiyah, Al-Jubailah, Al-Diriyah, Al-Ha'ir, and Al-Kharj. The valley ends in the Al-Kharj depression, with Wadi Al-Sulay and Wadi Nisah also ending in this depression. From 52 m in the east, where the valley terminates at Sabkhat Al Hamr, to 1504 m in the west, where the central Saudi Arabian highlands are located, the valley's surface level varies; 1452 m is the topographical extent of the valley. Less than 100-m-high regions make up 0.1% of the valley's total area, and less than 500-m-high parts make up 14.6%. Moreover, 9.3% of the valley is made up of areas that are higher than 1000 m. The valley's surface slope is 1.9°, with highlands on its boundaries reaching 50.9°. The valley's slope is estimated to be less than 2°, with 17.8% of its area having a slope below 2°, 66.9% having a slope below 5°, 85.5% having a slope below 5°, and 0.6% having a slope above 30°.

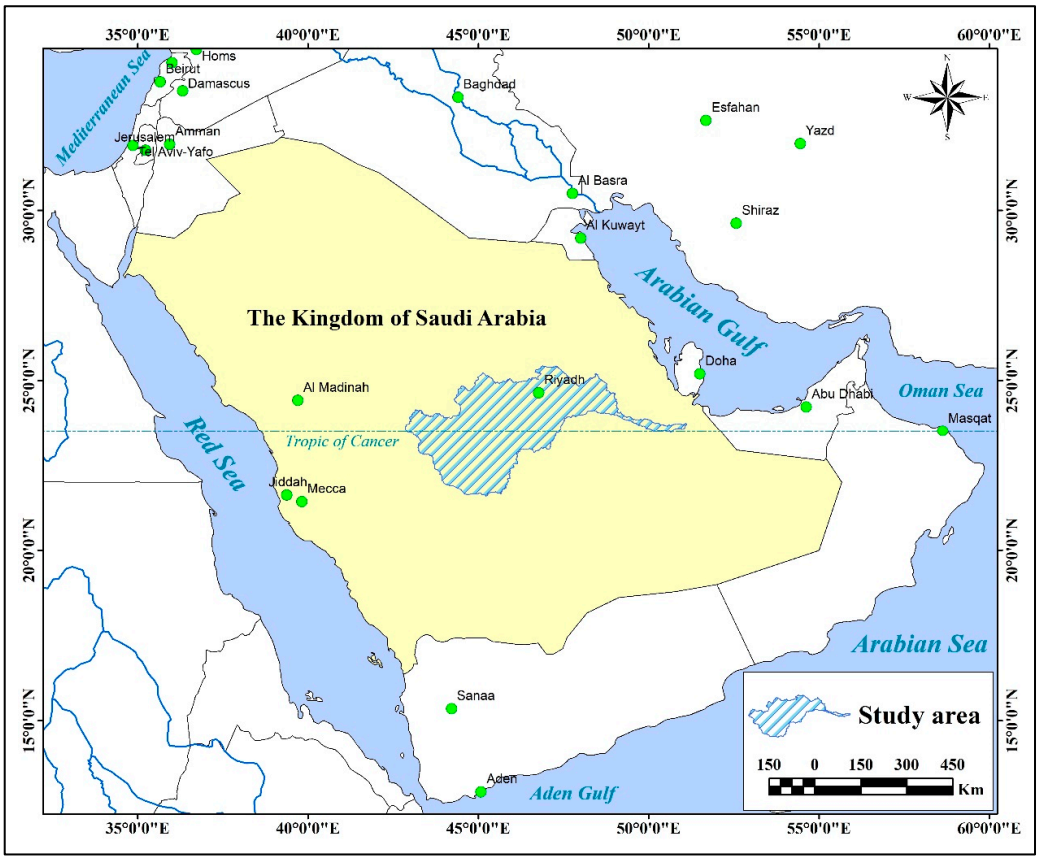


Figure 1. Location map of the study area.

2.2. Datasets

2.2.1. PERSIAN Data

This study aims to calculate the infiltration rates of surface water from rainfall into the ground to feed groundwater reservoirs in central Saudi Arabia, requiring the use of rainfall data for this calculation. Meteorological data from regional stations are highly inaccurate in calculating water volume and infiltration due to its limited coverage at specific locations. The study required continuous, spatially extended data to extract rainfall values in the entire area. As it is a crucial database for assessing the region's weather patterns, PERSIAN data are used as rainfall datasets [91]. The PERSIANN-CCS-CDR is a long-term dataset designed to provide accurate precipitation estimates from 1983 to present, offering 0.04° spatial and 3-hourly temporal resolution, making it a reliable tool for extreme event detection and providing a reliable long-term solution [92].

Traditional precipitation datasets usually force a choice between high-resolution short-term data or low-resolution long-term records, often failing to capture extreme weather accurately. PERSIANN-CCS-CDR resolves this by providing high-resolution, long-term data. It merges the PERSIANN-CCS and CDR algorithms, utilizing geostationary satellite and NOAA infrared data, and applies GPCP bias adjustments to ensure precision [56,62,81,93,94]. Public access to this dataset is provided via the NOAA National Centers for Environmental Information (NCEI) and the Center for Hydrometeorology and Remote Sensing (CHRS) data portal. The PERSIANN-CCS-CDR datasets are used to calculate rainfall amount in the study area for 10 years for the period (2013–2022).

2.2.2. Digital Elevation Models (DEM)

Digital elevation models (DEMs) are essential components of remote sensing and photogrammetry, serving as a core layer in spatial data infrastructure and national, regional, and continental topographic databases [95]. There is an increasing focus on quantifying land surface topography to better understand the complex interactions between Earth's dynamic systems, such as atmospheric, geomorphic, hydrologic, and ecological processes [96]. As stated by [97,98], topography serves as an essential constraint and boundary condition across multiple fields. It is critical for modeling flood risks and runoff, understanding atmospheric boundary layer friction, and conducting research on global environmental change and regional sustainable development. The growing need for wide-area DEMs, such as TerraSAR-X and TanDEM-X, and global elevation data from the GEDI satellite altimeter mission has surged. The increasing use of DEMs in topographic analysis has facilitated a deeper understanding of geomorphic processes and landforms, as well as improved height and biomass mapping [99]. DEMs are crucial in GIS for digital relief maps, mapping, geospatial visualization, orthophoto generation, and three-dimensional analysis in hydrology, environmental modeling, urban planning, and geology, serving as the basis for digital relief maps, and are essential for various applications [100]. This study utilizes data from the Shuttle Radar Topography Mission (SRTM), a collaborative project involving NASA, the National Geospatial-Intelligence Agency, and the space agencies of Germany and Italy. The mission captured topographical data using C-band and X-band synthetic aperture radar (SAR) interferometry from antennas mounted on the space shuttle Endeavour. The mission took place from 11 to 21 February 2000, imaging the Earth's surface between 60°N and 56°S, covering 80% of the Earth's landmass. The longer wavelength of SAR allows for smaller particles to be transmitted, while the higher signal-to-noise ratio validates C radar processing and quality control [101–103]. The digital elevation models are used to extract the Wadi AS SAHBAA catchment area and the subbasins of AS SAHBAA, which are used to calculate surface water seepage into groundwater (Figure 2).

2.2.3. Geology

The geographical location of the study area, situated in the central Arabian Peninsula, enhances its geological diversity through its combination of highlands, plains, and valleys, which expose various geological layers that are crucial for the recharge of the region's groundwater reservoir (Figure 3). The exposed rocks play a crucial role in the mechanisms of water seepage, specifically in recharge processes from the surface to the underlying substratum. The permeability of these lithologies significantly influences surface water flow; it facilitates easier movement through permeable rock types while hindering flow in more compacted formations. Consequently, the geology of the surface terrain directly impacts groundwater recharge (GWR) dynamics. Surface geological formations can be summarized as follows:

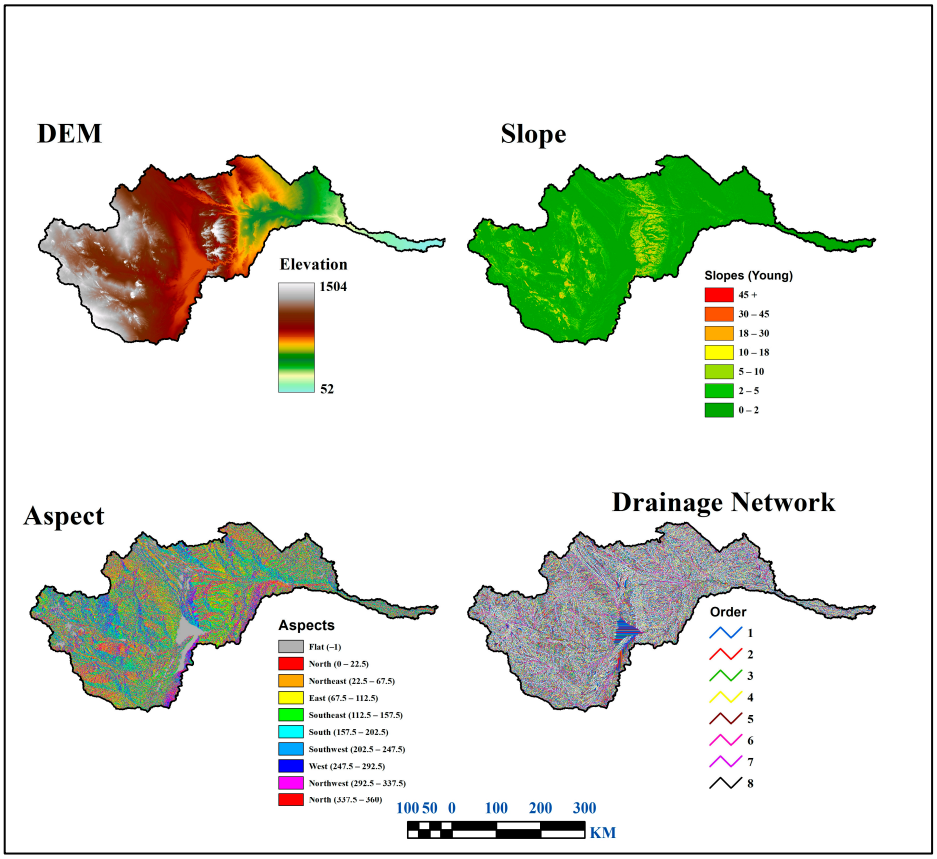


Figure 2. Surface Topography and Drainage Network.

- Precambrian Basement: The crystalline basement, primarily of Precambrian age, is composed mostly of granitic rocks, including various granites, granodiorite, diorites, and granite-gneisses of both plutonic and ultra-metamorphic origins [91]. The rocks from this era exhibit impermeability, meaning they do not allow water to pass through them.
- Permian Rocks: The formations from this era in the study area are characterized by the presence of the Khuff formation. The sequence consists of four equal units, starts with limestone and dolomite, unfossiliferous shale, limestone with gypsiferous shale, and colored beds with petrified wood [104]. Good porosity has been observed ranging from 4% to 18%, while the permeability ranges from 5 to 20 millidarcies (mD) [105].
- Permian–Triassic: this era represents the study area in Sudair shale, which predominantly consists of sandy claystone. The lower section is composed of dark-red massive shale. The upper section features calcareous siltstones and silty, impure limestones [106]. The Sudair formation's permeability values are typically less than 0.01 mD, indicating poor reservoir quality [107].
- Triassic Rocks: this section of the surface geology in the study area is represented in the Jilh formation, which is primarily composed of clastic-rich mudrocks and anhydrite from sabkha environments, interlayered with dolomitized carbonates [108]. The Jilh Formation, a tight Triassic formation, is characterized by its low porosity and permeability.
- Triassic–Jurassic: Minjur sandstone is the Triassic–Jurassic formation in the study area and is a Buff sandstone, ranging from fine to coarse grained, that often exhibits crossbedding and can be calcareous, breaking down into small spherical concretionary masses [109]. The permeability of Minjur sandstone is primarily determined by its porosity, with levels reaching up to 34% and permeability of up to 3000 mD [110].

- Jurassic Rocks: Jurassic marine rocks in central Saudi Arabia extend in a concave arc westward, with a maximum thickness exceeding 1000 m. They are categorized into six formations: Marrat, Dhurma, Tuwaiq Limestone, Hanifa, Jubaylah, and Arab formations. Aphanitic limestone is the predominant rock type mentioned, accompanied by subordinate amounts of shale, sandstone, calcarenite, dolomite, and some anhydrite.
- Cretaceous Rocks: It consists of six formations: Sulaiy, Yamama, Buwaib, Biyadh, Wasia, and Aruma. These formations consist of chalky aphanitic limestone and biogenic calcarenite interbedded with fine sandstone at the top. The limestone section includes subordinate dolomite and shale, with a lower portion that transitions to sandstone [111].
- Tertiary Rocks: these formations are represented in two formations: Umm er Radhuma and Kharj, which consists of limestone, including dolomitic limestone and dolomite, found alongside lacustrine limestone, gypsum, and gravel.
- Quaternary Deposits: These are found in the study area in three types: Sabkha deposits, which consist of salts, gypsum, and clay; Fluvial deposits, which consist of silt, sand, and gravel; and Aeolian deposits, which consist of fine sand (dunes).

2.2.4. Soil Type

The soil types identified in the study area play a significant role in controlling groundwater recharge, infiltration, and permeability processes. Lithosols are characterized by very shallow depth over hard rock, which severely limits water infiltration and results in very low groundwater storage capacity. Regosols, including calcareous regosols (Qc) and calcaric regosols (Rc), generally exhibit moderate infiltration due to their loose and weakly developed structure; however, the presence of calcium carbonate may reduce permeability over time (Figure 3). Yermosols, such as haplic (Yh), calcic (Yk), and luvic (Yl) types, are typical desert soils with low organic matter content and limited profile development. In particular, calcic yermosols contain a calcic horizon that restricts deep percolation, while luvic yermosols show clay accumulation that reduces permeability but may enhance moisture retention in the upper layers. Additionally, solonchaks (Zo) are high saline soils with poor structure, leading to very low infiltration rates and limited groundwater recharge. Overall, these soil characteristics indicate low to moderate permeability and weak groundwater storage potential, which, in turn, increases surface runoff and reduces deep infiltration in arid environments. The FAO soil types in the study area are the following:

- Lithosols (I): Lithosols are very shallow soils that occur directly over hard rock. They have extremely limited soil development, low water-holding capacity, and are generally unsuitable for agriculture due to their thin profile and poor fertility.
- Calcareous Regosols (Qc): Calcareous regosols are weakly developed soils that contain a high proportion of calcium carbonate. They are typically found in arid and semi-arid environments and are characterized by a loose structure and limited horizon differentiation.
- Calcaric Regosols (Rc): Calcaric regosols are similar to other regosols but are specifically enriched with lime (calcium carbonate). These soils are young, poorly developed, and often exhibit low organic matter content and weak structure.
- Haplic Yermosols (Yh): Haplic yermosols are typical desert soils with minimal horizon development. They are dry, coarse-textured, and very low in organic matter, reflecting the harsh climatic conditions under which they form.
- Calcic Yermosols (Yk): Calcic yermosols are desert soils characterized by the accumulation of calcium carbonate within the soil profile, forming a calcic horizon. This accumulation affects soil permeability and root penetration.

- Luvic Yermosols (Yl): Luvic yermosols are desert soils that show evidence of clay accumulation (argillic horizon). This results in some degree of profile development compared to other yermosols, influencing water retention and soil structure.
- Solonchaks (Zo): Solonchaks are saline soils with a high concentration of soluble salts. They commonly occur in arid and coastal regions where evaporation exceeds precipitation, leading to salt accumulation. These soils pose significant limitations for plant growth.

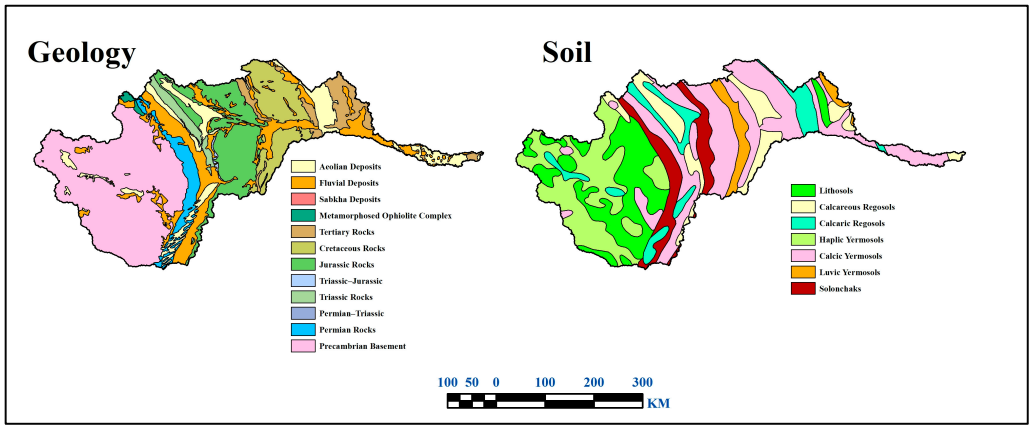


Figure 3. Surface Geology and Soil Types.

2.3. Methods

In order to better understand how water moves through drainage basins and leaks into groundwater reservoirs, the study tracks water movement in the study region from cloud formation to rainfall. Three steps comprise the methodology: monitoring clouds, assessing danger, and calculating surface water seepage rates to replenish reservoirs. Figure 4 shows the flow chart for methodology framework of the study. To research weather and climate components using remote sensing systems like the NOAA satellite, satellite imagery is essential. The density, temperature, and pressure distribution of atmospheric strata may be defined mathematically using satellites.

2.3.1. Extract and Calculate Rainfall Amount

The PERSIANN project, under California University, uses neural network models to extract rainfall data from satellite imagery, analyzing and modeling digital files from 2013 to 2022 to understand spatiotemporal variations in rainfall and its impacts on groundwater reservoirs. The development of PERSIANN-CCS-CDR begins by extracting rain rate (RR) data from the PERSIANN-CCS model, which estimates precipitation using global infrared (IR) imagery. The IR input data transitions from GridSat-B1 (1983–February 2000) to higher-quality CPC-4km data (March 2000–present) to ensure improved output accuracy.

In the next step, the 0.04-degree resolution grids are filtered using a 0.1 mm per 3-h threshold to remove spurious light rainfall signals before being aggregated into monthly totals. Finally, these high-resolution monthly accumulations are resampled to a 2.5-degree resolution using bilinear interpolation, enabling direct spatial matching with the GPCP v2.3 dataset for calibration.

$$R_{Cum-PERSIANN-CCS}(i' - j') = \sum^{nd} \sum^{nh} \left\{ \sum^{62} \sum^{62} r - PERSIANN - CCS(i' - j') \geq thd \right\} \quad (1)$$

where $R_{Cum\text{-}PERSIANN\text{-}CCS}$ and $r_{\text{-}PERSIANN\text{-}CCS}$ are monthly 2.5° aggregated PERSIANN-CCS estimates and 30 min/3-hourly *PERSIANN-CCS* estimates at 0.04° spatial resolution; i

and j are the latitude and longitude; *nd* and *nh* are the number of days and the number of 30 min/3-hourly *PERSIANN-CCS* samples in each day. The bias adjustment weights for every monthly 2.5° grid cell are determined in the following step:

$$w\left(i', j'\right) = w\left(i, j\right) \times R_{GPCP}\left(i', j'\right) / R_{Cum-PERSIANN-CCS}\left(i' - j'\right),\ 0 \leq\ w \leq\ 25, \quad (2)$$

where *RGPCP* is the monthly rain rate of *GPCP* for a given pixel. For additional processing, the 2.5° weight grids are bilinearly interpolated to a spatial resolution of 0.04°. Experiments showed that weights may grow unreasonably enormous in places with minimal monthly rainfall, especially at high latitudes and desert regions, leading to unrealistically high 3-hourly rainfalls. A maximum weight of 2.5 is imposed in order to lessen this. The monthly weights at 0.04° are added to each initial input rainfall rate (RR) grid in the last two phases, with modifications made depending on whether the data came from 3-h or 30-min IR intervals, using the following equation:

$$PERSIANN - CCS - CDR\left(i, j\right)\ = w\left(i, j\right)\ \times\ r - PERSIANN - CCS\left(i' - j'\right) \quad (3)$$

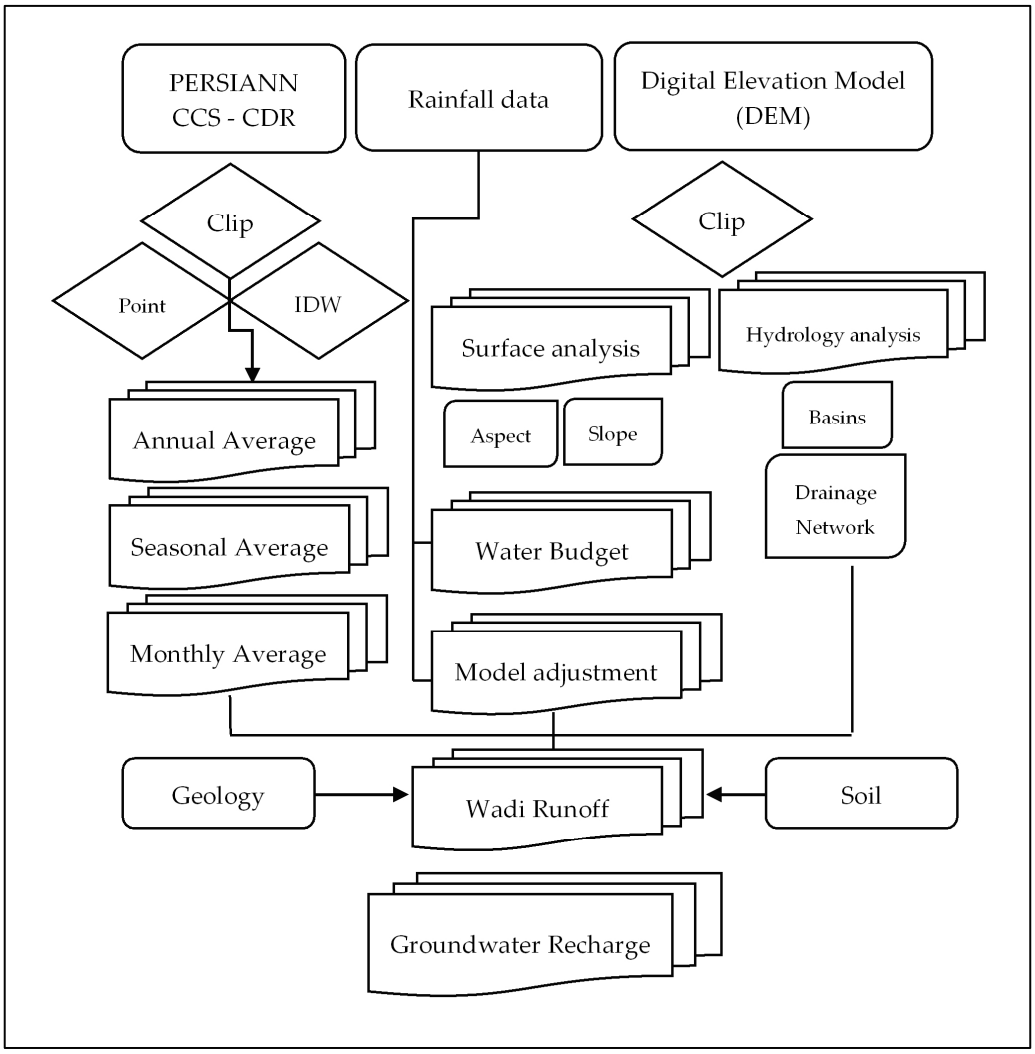


Figure 4. Proposed methodology of the study.

The study used 120 digital images from the *PERSIANN-CCS-CDR* dataset, which were then clipped using the outer borders of Wadi AS SAHBAA. The resulting file was converted into a point feature class; about 7667 points cover all the AS SAHBAA basin, which are

interpolated using IDW algorithm and extraction of monthly rainfall maps. The database for vector data was run in WGS 1984 coordinate system zone 39 north, and the output cell size was 1 km; the pixel with no rain data takes the value zero. The sub basins were used to calculate the minimum, maximum, and mean of the groundwater recharge and also the total volume of infiltration. The region's data from the Riyadh Meteorological Station were used to determine the highest single-day rainfall. After that, digital files were uploaded for these storms' dates over a single day.

2.3.2. Calculate Groundwater Recharge Rate

Rainwater that has seeped in replenishes the aquifer and replaces the soil's moisture deficit. Due to evaporation, transpiration, and runoff from the watershed, part of the precipitation that reaches the earth may not completely permeate or contribute to the groundwater. Groundwater recharge estimation can be achieved through various manual or automated methods of baseflow separation [112]. Groundwater recharge is typically estimated through water balance/water budget models, which consider the fluctuation in well water levels and the specific yield of aquifer material [113]. The groundwater balancing approach is a good way to measure groundwater recharge and gauge how accurate other approaches are at measuring groundwater losses and recharge [114–116]. Various empirical connections between recharge and rainfall derived for various places with comparable climates were used to evaluate rainfall recharge. Statistical studies suggest that approximately one-third of the water applied to soil annually permeates to the water table [117,118]. There were several methods for estimating the groundwater recharge. Singh (1973) [119] proposed an equation for calculating recharge from rainfall:

$$Q_r = \{C_r - (R_o + E_t)\} \times A_c \quad (4)$$

where Qr is the volume of the water available for recharge, Cr is the contributing part of the rain, Ro is the direct runoff, Et is evapotranspiration, and Ac is the area of the catchment. Penman developed an equation to estimate evapotranspiration by integrating the mass transfer method with energy balance using data on temperature, sunshine, relative humidity, and wind speed. This equation is as follows:

$$ET = \frac{\Delta\,(R_{ni} - G_i) + \rho_a \frac{e_{si} - e_{ai}}{r_{ai}}}{\Delta + \gamma\left(1 + \frac{r_{si}}{r_{ai}}\right)} \quad (5)$$

where *Gi* is the soil heat flux, R_{ni} is the net radiation from the surface, (*esi* − *eai*) is the air's vapor pressure deficit, *rai* and *rsi* are the aerodynamic and surface resistances, *ρa* is the mean air density at constant pressure, *cp* is the air's specific heat, Δ is the slope of the saturation vapor pressure–temperature relationship, and γ is the psychrometric constant. Using Equation (5), the FAO Penman–Monteith equation was developed to estimate ETo:

$$ET_o = \frac{0.408\Delta(R_{\,n}G) + \gamma\frac{T+27}{900}\,u2\,(e_s - e_a)}{\Delta + \gamma\,(1 + 0.34_{u2}\,)} \quad (6)$$

where ET_o is evapotranspiration, R_n is net radiation, G is soil heat flux density, T is the mean daily air temperature, u_2 is the wind speed, e_s is saturation vapor pressure, e_a is actual vapor pressure, $e_s - e_a$ is saturation vapor pressure deficit, Δ is slope vapor pressure, γ is psychrometric constant. Among various methods for estimating evapotranspiration, the Penman–Monteith equation is the standard reference approach.

The variability in groundwater recharge from rainfall is influenced by soil type and geological conditions. For granite, the annual recharge is modeled as Rech = {0.172 (RF)–44},

while for alluvial soil, it is Rech = {0.147 (RF)–6} [120]. Additional relationships between annual recharge and rainfall have been proposed by Chandra and Saxena (1975) [121]:

$$Rech = 3.984\ (RF - 40.4)^{0.5} \quad (7)$$

where RF is rainfall (mm). Tonder and Kirchner (1991) [122] found a correlation between groundwater recharge and rainfall in South Africa's Karoo formations. They used a triangular finite element network to assess aquifers' relative saturated volume fluctuations, revealing that recharge in Karoo formations is about 2% to 5% of annual rainfall. The Tonder and Kirchner recharge formula is

$$Re = 0.024\ (P - 51)\ (\text{mm}) \quad (8)$$

where R_e is groundwater recharge, and P is precipitation.

The previous equations were used to calculate groundwater recharge rates in the study area from rainwater across 7667 cells covering the basin. Calculating groundwater recharge at the point level for each year of the study yielded three values: maximum, minimum, and average, which are presented in Table 3. The average groundwater recharge rate in each equation was used to calculate the volume of groundwater recharge across the 126 basins studied. The minimum value represents the product of the average recharge volume in the smallest basins, the maximum value represents the product of the recharge volume in the largest basins, and the average represents the average recharge volume across all 126 basins in the region. This process was repeated by applying the three selected methodologies to the basins throughout the study period (2013–2022).

Leakage during the lag time is known as the leakage that occurs at the onset of rainfall and continues until the water appears on the surface of the earth and begins to flow. (Wilson, 1980) [123] uses the sub-basin characteristics such as basin area, topography, stream length and number, lag time, and discharge time to estimate infiltration to the groundwater, as follows:

$$LT_L = a \times T_L \times 0.08\ \text{mm/min} \quad (9)$$

$$T_L = 0.6 \times T_C \quad (10)$$

$$T_C = 0.0078 \times \frac{L^{0.77}}{S^{0.38}} \quad (11)$$

where LT_L is leakage during the lag time, T_L is lag time, 0.08 mm/mi. is the average amount of leakage for all types of surface sediments, T_C is time of concentration, L is the mainstream length (m), and S is the elevation difference.

Seepage or leakage during discharge time m^3 reflects the amount of leakage within the bed rock that lies beneath the surface soil sediments that cover the sides and bottoms of the basin, which is calculated through the following equation:

$$S_e = a \times T_d \times 0.158\ \text{mm/min.} \quad (12)$$

$$T_d = \frac{0.305\ L^{1.15}}{7700\ (0.305 S^{0.38})} \quad (13)$$

where S_e is seepage, T_d is basin discharge time, 0.158 mm/mi. is constant expressing the original rock type, L is the mainstream length (m), and S is the elevation difference. The total basin infiltration is calculated as the following equation:

$$B_L = LT_L + S_e \quad (14)$$

where B_L is total basin infiltration, LT_L is leakage during the lag time, and S_e is seepage.

3. Results

3.1. Rainfall Estimates from Satellite Imagery

3.1.1. Annual Precipitation

The average annual precipitation in the study area was 116.6 mm/year during the study period (2013–2022). This value reflects the arid conditions that characterize the region compared to other parts of Saudi Arabia, particularly the southwest, where annual precipitation exceeds 200 mm, as in the city of Abha in the Asir region [29]. Annual precipitation exhibited variability throughout the study period, characterized by fluctuations that were influenced by the frequency and intensity of rainstorms affecting the region. Specifically, the year 2019 recorded the highest annual precipitation, totaling 222.3 mm. This peak was attributed to elevated rainfall rates resulting from multiple rainstorms passing through the area. On the other hand, 2021 experienced the lowest annual precipitation, which was significantly impacted by the COVID-19 pandemic. The pandemic led to a marked decline in the number of rainstorms impacting the region, contributing to a drop in overall precipitation levels. Fluctuations in annual precipitation throughout the study period exhibited significant variability with changes ranging from 13.6% to 104.9%. Notably, there was a pronounced increase in precipitation between 2018 and 2019, marking a peak in rainfall activity for the region. However, this trend was sharply reversed in 2020, when annual precipitation plummeted by 59.6%. This dramatic decrease was attributed to the disruption of human activities during the COVID-19 pandemic, which saw its peak in 2021. Figure 5 illustrates the geographical distribution of rainwater concentration within the Wadi AS SAHBAA basin. The data reveal a pronounced concentration in the northern, eastern, and central regions of the basin, while a noticeable decrease in rain concentration is evident in the western and far eastern areas. This pattern highlights the substantial influence of surface topography on rainwater distribution across the basin.

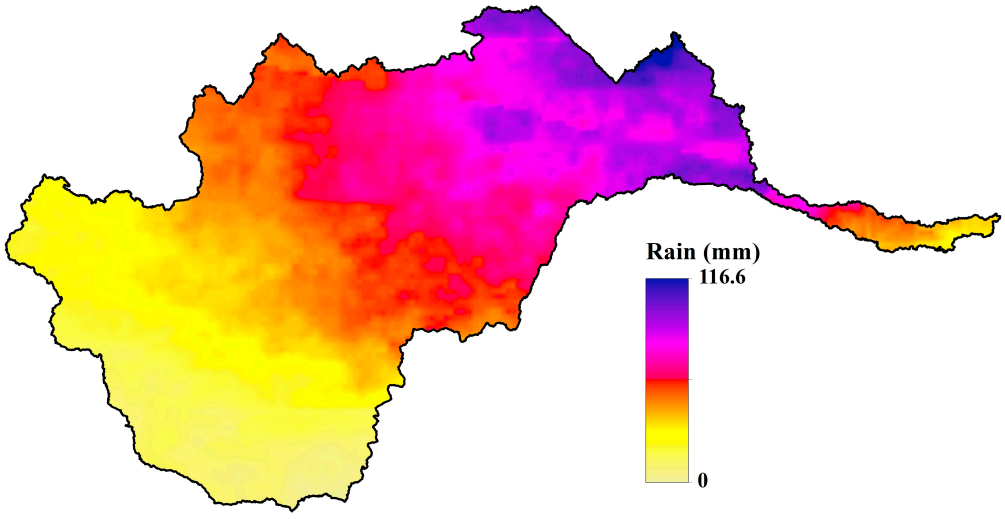


Figure 5. Annual Precipitation Rate for Wadi AS SAHBAA (2013–2022).

3.1.2. Mean Annual Precipitation

The mean annual precipitation in the study area is 9.7 mm per year; this rate increases in years with high precipitation rates and in months with increased quantity and quality of rainstorms. The study's annual change in mean annual precipitation in the Wadi AS SAHBAA reveals 2019 as the highest year, with 18.5 mm of rain (Table 1 and Figure 6). The table reveals fluctuations in expected rainfall in AS SAHBAA region from 2013 to 2022 with a significant increase in rainfall distribution from 2013–2019 due to numerous rainstorms, including the 18–19 March 2015 storm that caused 204 accidents in Riyadh and 8 injuries.

The study period saw two major rainstorms in Saudi Arabia: 29 November 2015, which flooded vehicles on the highway west of Riyadh causing schools to close for the second day, and 28 November 2016, which led to numerous landslides and traffic accidents, resulting in widespread flooding. The table shows a decrease in rainfall from 2020 to 2023, with 2021 experiencing the lowest mean annual precipitation of 4.5 mm. This is attributed to a decrease in rainstorms and cloud activity, which was largely due to the cessation of human activities during the COVID-19 pandemic. In 2022, the mean annual precipitation increased significantly, reaching 6.6 mm. This was largely due to several rainstorms, with the most notable being the December 10th storm, which raised the state's alert level to red due to the intensity of the rainfall and potential property losses.

Table 1. Annual and Seasonal Average Potential Precipitation for Wadi AS SAHBAA (2013–2022).

	Year	2013	2014	2015	2016	2017	2018	2019	2020	2021	2022	Ave.
Average	Year Ave.	10.2	6.6	8.4	10.6	8.0	16.3	18.5	7.5	4.5	6.6	9.7
	Total Rain	122.8	78.9	101.3	126.7	95.5	195.7	222.3	89.8	53.8	79.4	116.6
	Change (%)	-	−35.7	28.4	25.1	−24.6	104.9	13.6	−59.6	−40.1	47.6	−3.5
Seasonal	Winter	13.4	7.7	2.8	10.1	13.7	11.3	23.8	4.1	7.0	7.6	10.2
	Spring	14.9	9.3	19.7	28.6	14.2	19.8	41.0	16.4	5.8	6.4	17.6
	Summer	2.3	0.0	0.3	1.0	0.9	1.4	3.6	1.0	4.1	7.9	2.3
	Autumn	18.6	8.7	5.8	7.7	2.0	30.7	7.6	6.1	0.3	4.6	9.2

Note: Resource: PERSIANN–PDIR–NOW data analysis during 2013–2022.

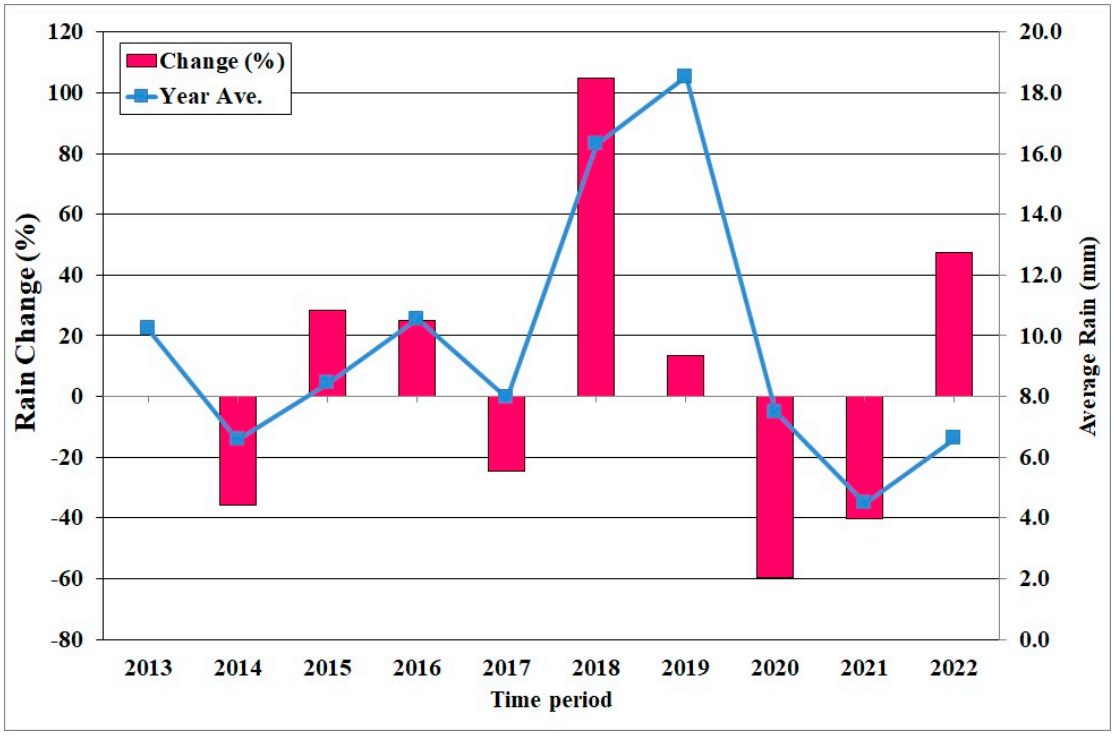


Figure 6. Mean Annual Precipitation for Wadi AS SAHBAA (2013–2022).

The study area experienced a −3.5% decrease in mean annual precipitation from 2013 to 2022 due to a decrease in strong rainstorm rates, primarily due to changes in the number and strength of rainstorms, which significantly increase in the spring and winter seasons each year. The spatial variations in the mean annual precipitation on the study area shows in Figure 7, revealing significant rainfall concentrations in the northern and eastern parts in

certain years and in the northern and western parts in other years. In 2013, the study period began with a mean annual precipitation of 10.2 mm, higher than the general average of 9.7 mm. Rainstorms were concentrated in the eastern and northern parts of the study area. This year, numerous rainstorms occurred, resulting in medium to light rainfall. In 2014, the region experienced a decrease in mean annual precipitation, reaching 6.6 mm, which was below the average, primarily due to concentrated rainfall in the northern and western areas, The change percentage during this period was −35.7%. In 2015, the mean annual precipitation increased by 28.4% to 8.4 mm, but it still fell short of the average during the study period.

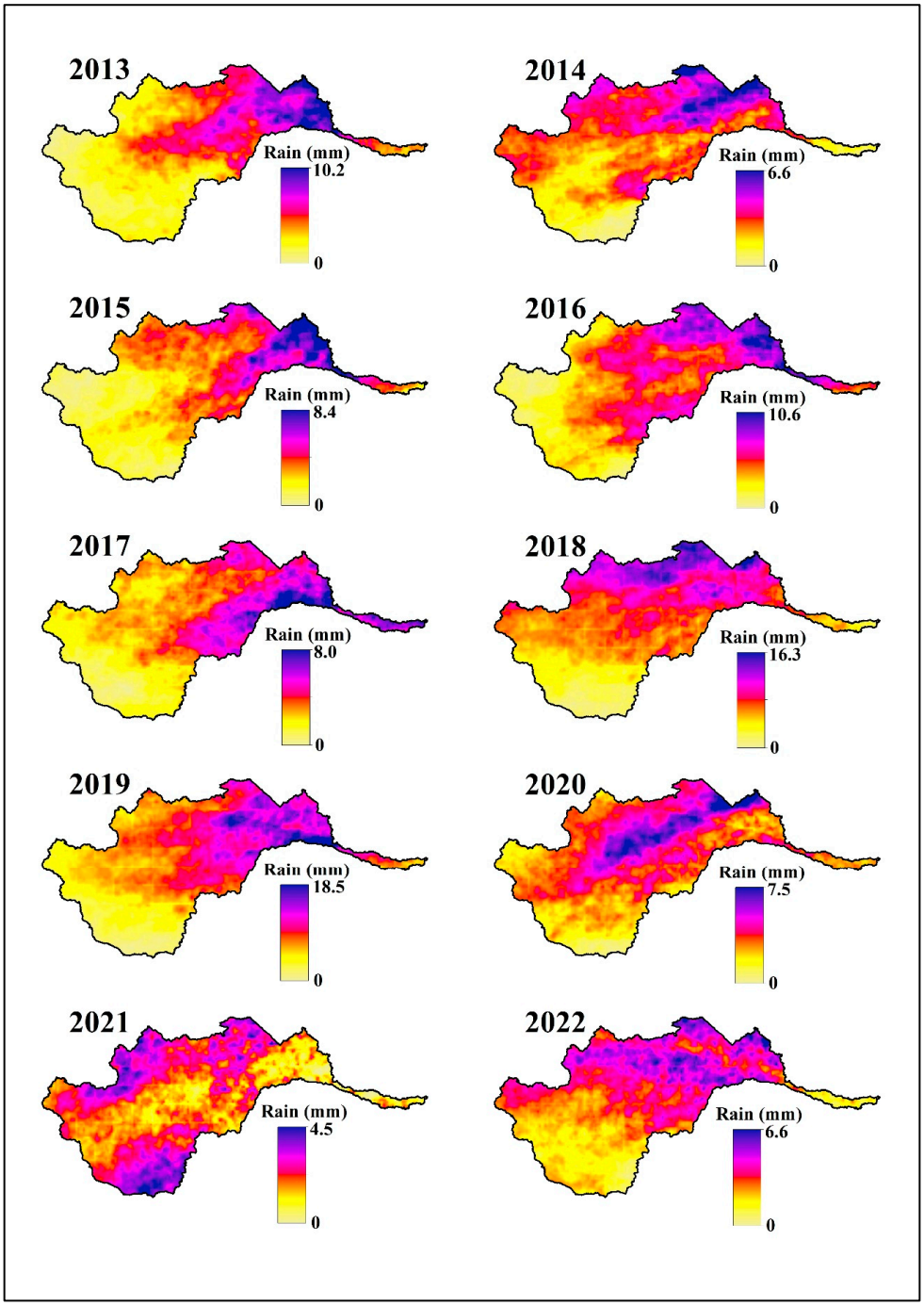


Figure 7. Spatio-Temporal Changes in Potential Precipitation Volume for Wadi AS SAHBAA (2013–2022).

Most of the rainfall was concentrated in the eastern region, away from inlets. With a change rate of 25.1%, the study area's mean annual precipitation climbed to about 10.6 mm in 2016. This is explained by the fact that there were a lot of rainstorms that year, the most significant of which were on 28 February and 31 March. A decrease in the number of rainstorms throughout 2017 caused the mean annual precipitation to drop by 24.6% to 8.0 mm, with most of the rainfall occurring in the southern portion of the basin. A rise of 104.9% from the previous year, the mean annual precipitation climbed to about 16.3 mm in 2018. This was because there were more rainstorms that year, with the 28 October 2018 downpour being the most notable. The basin's northeastern and northern regions received the most rainfall.

The mean annual precipitation in the study region peaked in 2019 with 18.5 mm per year, up 8.8 mm and 13.6% from the year before. Numerous heavy rainstorms that lasted more than a day, such as the storms that occurred on 10 February and 13 April, produced a lot of rain, which was mostly caused by vigorous wind and cloud activity. It should be mentioned that the eastern portion of the research area—more especially the lower portions of the basin—received most of the anticipated rainfall in 2019. The anticipated rainfall rates in 2020 dropped significantly to about 7.5 mm, with a change rate of −59.6%. Throughout the research period, the area had the highest rate of decline. In 2021, there was again another drop, with a mean annual precipitation of 4.5 mm and a change rate of −40.1%.

The study area experienced a significant decrease in rainstorms over the last two years, largely due to the global COVID-19 pandemic, its resulting curfew and suspension of movement, and its impact on weather conditions, including rain, which led to a sharp decline in rainfall. The study area experienced a decrease in mean annual precipitation in 2020 due to a decrease in storms, but some rainstorms occurred on 5 January and 17 April, with most of the rainfall concentrated in the central part of the region. The study found that 2021 had the lowest mean annual precipitation during the study period, with some rainstorms occurring in January and February primarily affecting the southwestern and northwestern sectors of the basin. In 2022, the mean annual precipitation increased by 47.6% to 6.6 mm, but this is still lower than the overall rainfall average in the region. Following the period of drop observed in 2020 and 2021, the year 2022 generally marks the start of rainfall activity in the region. It is seen that the passage of many rainstorms in the region—the most significant being the storms of 2 January 2022, 28 April 2022, and 19 December, 2022—has resulted in a concentration of the mean annual precipitation in the research area in the northern portion of the region.

3.1.3. Monthly Average Precipitation in the Study Area

The potential monthly average rainfall in the study area from 2013–2022, with November having the highest rate at 25.22 mm (Table 2). This is due to the end of autumn and the start of winter, when temperatures drop and atmospheric depressions pass over the northern parts of the Kingdom, particularly when some shift southward across central mountains.

Table 2. Monthly Averages of Maximum, Minimum, and Mean Precipitation Volumes in Wadi AS SAHBAA (2013–2022).

		Jan.	Feb.	Mar.	Apr.	May	Jun.	Jul.	Aug.	Sep.	Oct.	Nov.	Dec.	Year Average
2013	Min.	1	0	1	3	1	0	0	0	0	0	1	0	0.6
	Max.	58	34	37	62	42	37	15	17	0	0	215	23	45.0
	Mean.	9.9	4.4	10.8	25.4	8.4	2.4	2.5	2	0	0	55.8	1.2	10.2

Table 2. *Cont.*

		Jan.	Feb.	Mar.	Apr.	May	Jun.	Jul.	Aug.	Sep.	Oct.	Nov.	Dec.	Year Average
2014	Min.	1	0	1	1	0	0	0	0	0	0	1	0	0.3
	Max.	76	8	42	53	30	0	0	0	13	0	92	41	29.6
	Mean.	20.9	1	9	13.7	5.1	0	0	0	1.6	0	24.4	3.2	6.6
2015	Min.	0	0	8	0	1	0	0	0	0	0	0	1	0.8
	Max.	25	20	131	17	72	0	0	8	0	35	78	97	40.3
	Mean.	2.5	2.6	42.2	2.7	14.1	0	0	1	0	2.6	14.7	18.9	8.4
2016	Min.	0	0	5	16	0	0	0	0	0	0	0	0	1.8
	Max.	40	53	101	95	41	0	27	10	0	0	105	22	41.2
	Mean.	3.1	8.4	33.3	41.3	11.2	0	1.8	1.3	0	0	23.2	3.1	10.6
2017	Min.	0	4	2	1	1	0	0	0	0	0	0	0	0.7
	Max.	33	165	97	29	83	0	10	10	0	0	32	52	42.6
	Mean.	3.7	34.2	12.7	7.2	22.8	0	1.3	1.5	0	0	5.9	6.2	8.0
2018	Min.	1	1	1	15	0	0	0	0	0	1	9	0	2.3
	Max.	34	86	30	82	28	11	13	16	0	85	247	63	57.9
	Mean.	4.3	23.5	6.3	47.6	5.5	0.7	2	1.6	0	16.4	75.6	12.2	16.3
2019	Min.	1	1	5	6	7	0	0	0	0	0	1	0	1.8
	Max.	184	95	87	121	100	78	12	0	35	6	91	90	74.9
	Mean.	31.3	28	33.4	41.1	48.5	9.5	1.2	0	1.9	0.6	20.4	6.4	18.5
2020	Min.	0	0	1	3	1	0	0	0	0	0	1	0	0.5
	Max.	31	40	38	78	35	17	9	8	0	0	70	81	33.9
	Mean.	1.4	4.5	6.8	33	9.3	0.7	1.1	1.1	0	0	18.4	13.5	7.5
2021	Min.	0	1	0	1	0	0	0	0	0	0	0	1	0.3
	Max.	15	32	4	40	13	0	86	0	0	9	0	100	24.9
	Mean.	1.6	5.9	0.4	14.6	2.4	0	12.3	0	0	0.8	0	15.8	4.5
2022	Min.	0	0	0	2	0	0	1	0	0	0	0	1	0.3
	Max.	47	0	18	45	19	0	81	35	0	0	72	62	31.6
	Mean.	7.1	0	1.1	17.1	0.9	0	15.6	8	0	0	13.8	15.8	6.6
Month Average	Min.	0.4	0.7	2.4	4.8	1.1	0	0.1	0	0	0.1	1.3	0.3	0.9
	Max.	54.3	53.3	58.5	62.2	46.3	14.3	25.3	10.4	4.8	13.5	100.2	63.1	42.2
	Mean.	8.58	11.25	15.6	24.37	12.82	1.33	3.78	1.65	0.35	2.04	25.22	9.63	9.7

As November had high anticipated rainfall rates in 2018, roughly 75.6 mm; 2013, with 55.8 mm; and 2014, with around 24.4 mm, the monthly average rainfall in November was approximately 25.22 mm. With the onset of spring weather fluctuations and the simultaneous blowing of warm winds from the south, which fill the air depressions that pass through the northern parts of the kingdom and are attracted by the mountain ranges of central Saudi Arabia, such as Mount Tuwaiq, which cuts the region from north to south, April ranked second in terms of precipitation rates during the study period. April had significant rainfall amounts in 2018 with a potential rainfall of 47.6 mm, 2016, and 2019 with a potential rainfall of 41.1 mm. March ranks third with an average rainfall of 15.6 mm, marking the start of the highest rainfall season of the year. The average rainfall increased to 42.2 mm in 2015, a severe storm that extended over 18–19 March, and 33.4 mm in 2019, a severe storm on 31 March. The average rainfall rate also increased in 2016, with

33.3 mm. May, the fourth month with an average rainfall of 12.82 mm, marks the end of spring and the start of summer, the region's least rainfall season.

May saw high rainfall in 2019, with 48.5 mm, and a severe storm on 20 May. May also experienced heavy rainfall in 2017, with an average of 22.8 mm, and in 2015 with 14.1 mm. September, June, August, and October are the months with the lowest rainfall, marking the end of summer and the beginning of autumn. These months are characterized by high temperatures, dry conditions, and low rainfall chances, except for some showers. These rare, small rains do not affect flash flooding or groundwater reservoir recharge. Figure 8 illustrates the fluctuations in monthly rainfall in the region from 2013 to 2022, revealing an increase in spring, winter, and autumn rainfall rates and a decrease in summer.

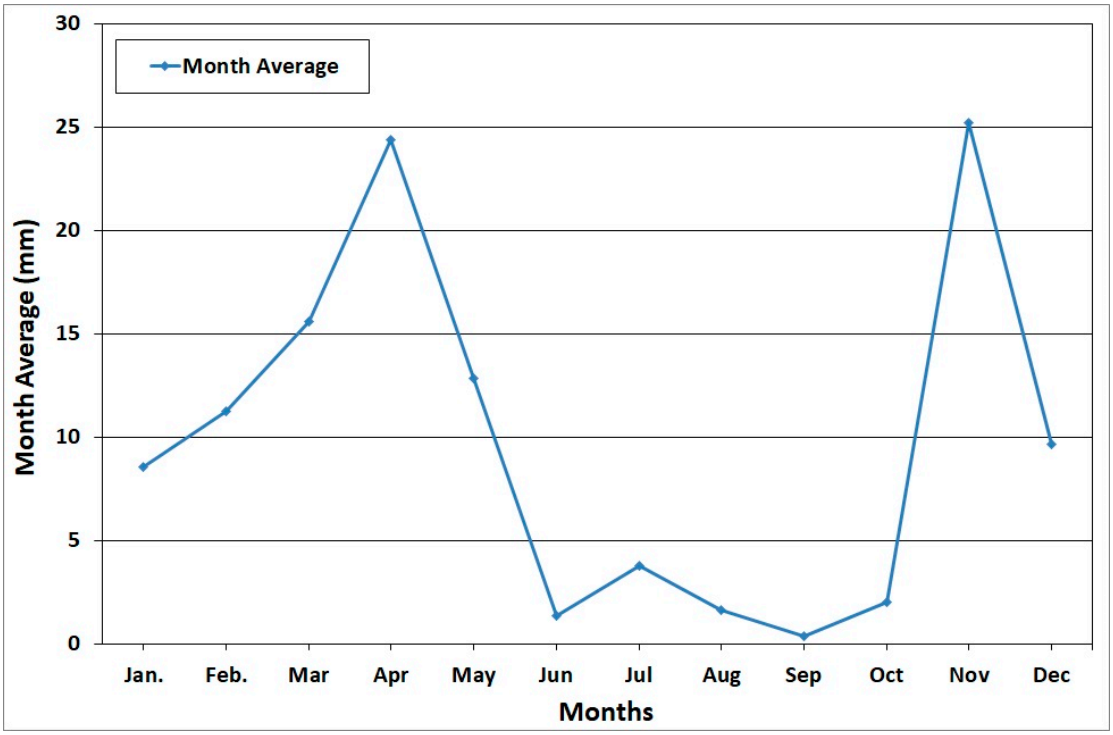


Figure 8. Monthly Variations in Potential Precipitation Volume for Wadi AS SAHBAA (2013–2022).

3.1.4. Seasonal Average Precipitation in the Study Area

Spring is the season with the greatest projected rainfall quantity, with an average of 17.6 mm over the study period, according to Table 1 and Figure 9, which display the prospective seasonal averages of rainfall in the study region for the period 2013–2022. In the spring of 2019, this quantity grew to 41.0 mm, which is mostly attributable to the rise in rainfall rates that occurred during this year due to the passage of several rainstorms and the occurrence of numerous weather changes. In the spring of 2016, it also hit 28.6 mm. Additionally, it is seen that the study area saw several rainstorms, the most significant of which were probably the ones that occurred on 28 October 2018, and 25 April 2018, which caused the average rainfall to rise to 19.8 mm in the spring of 2018. Rainfall is expected to increase this season due to the clear weather disturbances that have been observed, which are symbolized by the passage of air depressions in the northern part of the kingdom and the spread of monsoon winds, which have increased the likelihood of rainfall.

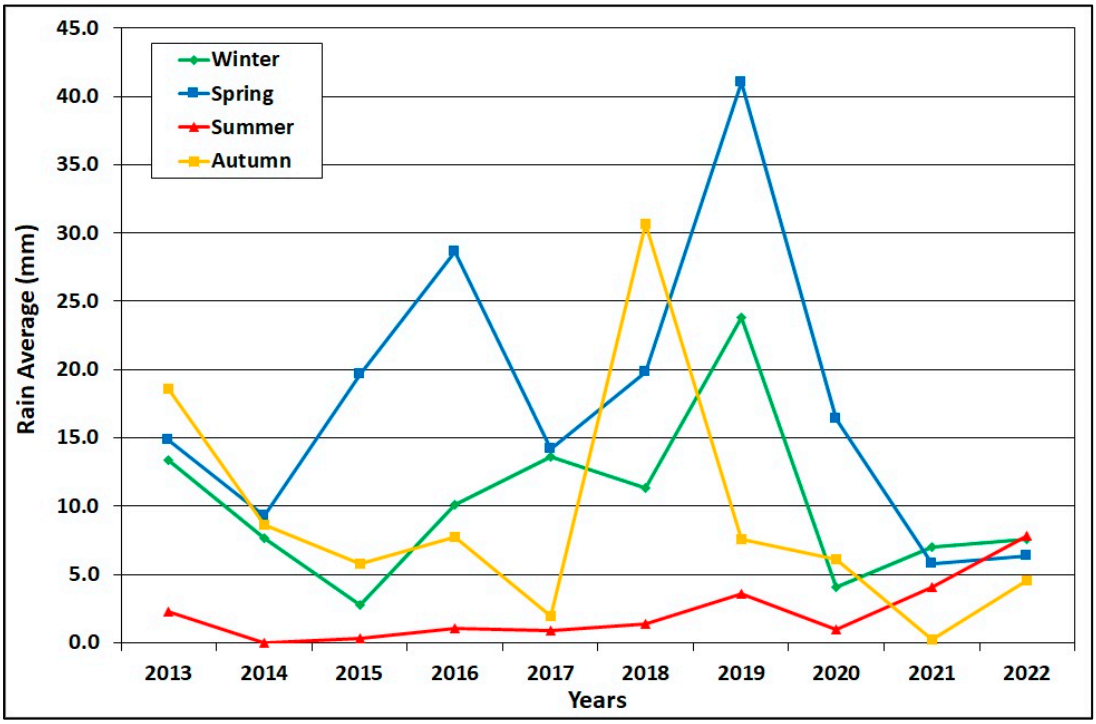


Figure 9. Seasonal Variations in Potential Precipitation Volume for Wadi AS SAHBAA (2013–2022).

Winter is the coldest season in Saudi Arabia, with an average of 10.2 mm of expected rainfall. Low-pressure systems frequently pass through the northern parts of the kingdom, potentially impacting the interior of the northern Najd Plateau and central Saudi Arabia, resulting in increased rainfall rates in the study area. The study area experienced its highest winter rainfall in 2019, reaching 23.8 mm, followed by 2017 at 13.7 mm and 2013 at 13.4 mm. The lowest was in 2015 at 2.8 mm, attributed to the intensity of low-pressure systems and their penetration into interior regions.

Autumn is the third most expected season, with an average of 9.2 mm of rainfall during the study period. It marks the transition between dry summer and rainy winter and is characterized by weather disturbances. One of the most dangerous floods occurred in November 2016, with the highest expected rainfall in 2018 reaching 30.7 mm, followed by 2013 at 18.6 mm. The study area experienced a surge in the intensity and quantity of rainstorms, leading to numerous flash floods. The study period in 2014 saw an average rainfall of 8.7 mm, which was higher than the seasonal average. Summer had the least amount of rainfall, averaging about 2.3 mm during the study. Summers in the research region are marked by severe heat, dryness, and humidity. Notably, summer rainfall in 2021 and 2022 was greater than the research period's general average for this season, with around 7.9 mm and 4.1 mm, respectively.

3.1.5. Monthly Average of Maximum Precipitation Volume During the Study Period

November is the month with the highest rainfall during the study period (2013–2022), primarily due to the large floods in 2018 caused by moderate heavy rains and thunderstorms on 16 and 23 November, resulting in numerous accidents and filling valleys with water (Table 2). The maximum recorded rainfall reached about 247 m. The monthly averages of the largest amount of rainfall are decreasing towards summer and autumn months. The highest rainfall recorded in December, January, and February was 56.9 mm, compared to 55.7 mm in spring, 39.5 mm in autumn, and 16.7 mm in summer. Winter is the season with the highest rainfall, with monthly averages of 100.2, 63.1, and 62.2 mm, respectively. Winter experiences high rainfall rates, with December and January having the highest amounts at 63.1 and

54.3 mm, respectively, accompanied by numerous heavy rainfall-causing rainstorms. The region experiences significant rainfall during autumn, with November being the most rainfall-prone month. The average rainfall increased from 100.2 mm in November 2018 to 247 mm in 2018, 215 mm in 2013, and 105 mm in 2016. The summer months in the study area experience low rainfall rates, averaging 16.7 mm. Some months experience absent rainfall due to high temperatures, severe drought, and the absence of low-pressure systems in the north. The year-round extension of Indian low-pressure systems to the east and the stability of a low-pressure mass in the Arabian Peninsula also contribute to this issue.

3.1.6. Monthly Average of Minimum Precipitation Volume During the Study Period

The average rainfall for the 2013–2022 study period is shown in Table 2. With an average of 4.8 mm, April was the month with the most rainfall. The highest rainfall was on 20 April 2016, with heavy clouds detected. The lowest rainfall was around 16 mm in that month. March had the second highest rainfall rate of 2.4 mm during the study period, while 2015 saw high rainfall rates of 8.0 mm. With an average of around 1.3 mm, November ranks third in terms of the lowest rainfall ever recorded, whereas an average of roughly 9.0 mm was anticipated in 2018. According to satellite imaging research, the season with the least amount of rainfall was spring, with an average of around 2.77 mm. Winter and autumn followed with averages of 0.47 mm and 0.03 mm, respectively.

3.1.7. Annual Analysis of Average Potential Precipitation Volume During the Study Period

The average annual precipitation in the Wadi AS SAHBAA basin during the study period (2013–2022) exhibited significant interannual and seasonal variability, as summarized in Table 2 and Figure 10. In 2013, the annual average precipitation was approximately 10.2 mm, with rainfall absent in September and October, yet peaking at 55.8 mm in November, 25.4 mm in April, and 10.8 mm in March. Several rainstorms occurred throughout the year, notably on 23 March, 26 April, and 16 November. Seasonal analysis indicated that autumn recorded the highest average precipitation (18.6 mm), followed by spring (14.9 mm), winter (13.4 mm), and summer (2.3 mm).

In 2014, the annual average decreased to 6.6 mm, representing a 35.7% reduction compared to the previous year, largely due to fewer rainstorms and rainy days. November was the wettest month with 24.4 mm, followed by January (20.9 mm) and April (13.7 mm). Spring received the highest seasonal rainfall (9.3 mm), followed by autumn (8.7 mm) and winter (7.7 mm), while summer remained dry. The following year, 2015, experienced an increase in annual precipitation to 8.4 mm, a 28.4% rise from 2014. Rainfall was absent in June, July, and September but peaked at 42.2 mm in March, 18.9 mm in December, and 14.7 mm in November. Spring remained the wettest season (19.7 mm), followed by autumn (5.8 mm), winter (2.8 mm), and summer (0.3 mm), with several severe rainstorms observed, including events on 18–19 March, 29 November, and 25 December. In 2016, the annual average increased by 25.1% to 10.6 mm, with April being the wettest month (41.3 mm), followed by March and November. Rainfall was absent in June, September, and October. Spring again received the most rainfall (28.6 mm), followed by winter, autumn, and summer. In 2017, although rainstorms were few, February experienced the highest monthly precipitation (34.2 mm), followed by May (22.8 mm) and March (12.7 mm). Seasonal averages indicated that spring received 14.2 mm, winter 13.7 mm, autumn 2.0 mm, and summer 0.9 mm.

In 2018, a substantial increase in annual precipitation was recorded, rising by 104.9% to 16.3 mm, mainly due to intense rainstorms, with November receiving the highest monthly average of 75.6 mm. Autumn recorded the highest seasonal rainfall (30.7 mm), followed by spring (19.8 mm), winter (11.3 mm), and summer (1.4 mm). The peak annual precipitation

occurred in 2019, reaching 18.5 mm, representing a 13.6% increase from 2018. May was the wettest month (48.5 mm), followed by April (41.1 mm) and March (33.4 mm), while August experienced no rainfall. Spring received the highest seasonal rainfall (41.0 mm), followed by winter (23.8 mm), autumn (7.6 mm), and summer (3.6 mm), highlighting pronounced interannual fluctuations.

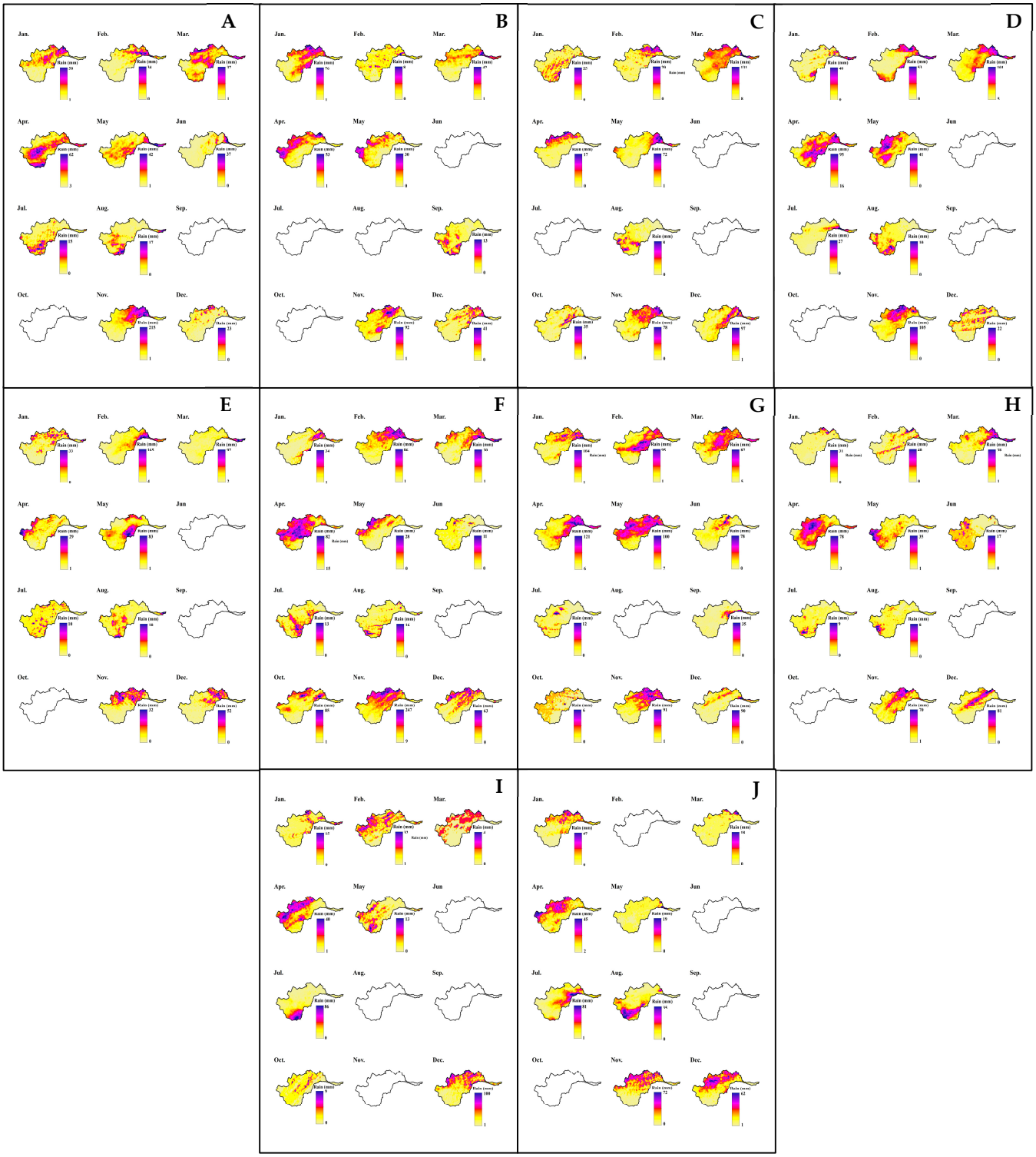


Figure 10. Expected Monthly Precipitation in Wadi AS SAHBAA (2013–2022), where (**A**) for 2013, (**B**) for 2014, (**C**) for 2015, (**D**) for 2016, (**E**) for 2017, (**F**) for 218, (**G**) for 2019, (**H**) for 2020, (**I**) for 2021, (**J**) for 2022. The months with no data refer to no precipitation were recorded.

In 2020, annual precipitation sharply decreased by 59.6% to 7.5 mm, influenced by changes in human activity and environmental conditions during the COVID-19 pandemic. April was the wettest month (33 mm), followed by November (18.6 mm) and December (13.5 mm). Seasonal averages indicated spring at 16.4 mm, autumn at 6.1 mm, winter at 4.1 mm, and summer at 1.0 mm. The lowest annual rainfall was recorded in 2021, with 4.5 mm, where December and April were the wettest months. Winter experienced the highest seasonal precipitation, followed by spring (5.8 mm), summer (4.1 mm), and autumn (0.3 mm).

In 2022, the annual precipitation increased by 47.6% compared to the previous year, reaching an average of 6.6 mm. Several rainstorms occurred, with the most notable on December 10, producing the highest daily rainfall of 36.9 mm at the Riyadh station. April recorded the highest monthly averages (17.1 mm), followed by December (15.8 mm) and July (15.6 mm), while February, June, September, and October experienced no rainfall. Seasonally, summer received the most rainfall (7.9 mm), followed by winter (7.6 mm), spring (6.4 mm), and autumn (4.6 mm).

3.2. Groundwater Recharge in Wadi AS SAHBAA

Three methodologies were applied to assess rainwater infiltration rates and groundwater recharge: the Tonder and Kirchner (1991) method, the Singh (1973) method, and the Chandra and Saxena (1975) method. The varying results indicated that the chosen calculation methods significantly influenced the outcome based on the input data. The findings were categorized into three distinct levels of infiltration. The first level, determined via the Tonder and Kirchner (1991) method, recorded a minimal rainwater infiltration rate of 1.59 mm, equating to 1.03% of total rainfall volume. The second level, as per the Singh (1973) method, showed an average infiltration rate of 11.86 mm, representing 9.3% of the rainfall volume. The highest level, established through the Chandra and Saxena (1975) method, revealed an average rate of 36.63 mm, capturing 28.5% of the rainfall volume. This comparative assessment highlights the variability in infiltration rates tied to different methodological approaches.

Based on the above; the average infiltration during 2013–2022 ranged between 1.59 mm and 33.63 mm, representing between 1.03% and 28.5% of rainfall volume. This is reflected in the storage volume of the region's groundwater reservoir, which ranges from 1.65 million m^3 to 38.27 million m^3 of water. Table 3 reveals that the infiltration rate in the study area varies annually, based on rainfall data from satellite images across the 7667 cells covering the area. It also varies due to the difference in the drainage basin areas, where the change in recharge rates was linked to rainfall values obtained from satellite imagery, while the recharge volume was linked to the size of the drainage basins.

In 2013, the mean average infiltration rate ranged between 1.79 mm and 42.68, resulting in 1.8 million to 44.8 million m^3 of water infiltration to feed the groundwater reservoir. Additionally, it is observed that the calculated infiltration average for the study area is lower than the overall average for the study period (2013–2022) in the following years: 2014–2015–2016–2017–2020–2021, 2022, and higher than the overall average in the following years: 2013–2018–2019.

The infiltration rate percentage fluctuates across the research region, peaking during years with heavy precipitation (1.78–10.8–30.4% of the total rainfall in 2019 and 1.69–10.6–30.3% of the total rainfall in 2018). In low-rainfall years, it falls, hitting 0.07–7.2–24.6% in 2021—the study area's lowest rainfall year—and 0.64–8.5–25.6% in 2014. Moreover, 2019 had the greatest infiltration rate and, as a result, the largest amount of groundwater seepage. The reason for this was the higher rainfall in this year, which had the largest precipitation volume in the study. The mean infiltration rate increased to about 4.18–24.62–54.83 mm in 2019. The AS SAHBAA sub-basins have seen a rise in mean infil-

tration volume, which ranges from 4.3 million m^3 to 57.3 million m^3. Groundwater seepage and infiltration rates declined in 2021 because of the research area's lowest rainfall year. With a range of 0.1 mm to 21.58 mm, the average infiltration rate was 8.6 mm. Water leaking into groundwater as a result ranged from 0.1 million m^3 to 22.5 million m^3, typically 9.0 million m^3 for the three methods. All of the aforementioned illustrate how the COVID-19 epidemic has affected precipitation and cloud cover, which is reflected in water recharge to groundwater reservoir.

The AS SAHBAA basin's average annual infiltration volume ranged between 1.65 and 38.27 million m^3, increasing with high rainfall years. Furthermore, 2019 saw between 4.3 and 57.3 million m^3 and 2018 between 3.7 and 51.0 million m^3, the highest in the region. In 2013, 1.8 million m^3 to 44.8 million m3 was recorded. However, groundwater infiltration volume is below average. However, the area of the sub-drainage basins affects the infiltration volume; bigger basins have higher infiltration volumes than smaller basins. The study found that infiltration in small basins ranged from 29.53 to 681. 5 thousand m^3, which is higher than the average in 2013, 2018, and 2019, while in large basins, it ranged from 38.83 to 896.42 million m^3, increasing to 102.3–1341.86 million m^3 in 2019 and decreasing to 2.45–528.13 million m^3 in 2021. It should be noted that the estimates overlook the morphometric, topographic, and hydrological features of these basins and assume that rainstorms affect the entire basin area, which is not the case due to natural processes.

The AS SAHBAA basin's geographical distribution of infiltration rates is depicted in Figure 11, where it is observed that both the geographical distribution of infiltration sites throughout the valley and infiltration rates varied yearly during the research period. It is often observed that the middle and lower areas of the basin, which correspond to the water gathering regions along the basin, have the highest infiltration rates. Additionally, these regions are the highest locations in the basin with the highest rates of rainfall. As can be seen from the figure, 2019 had the highest infiltration rates, with the highest value concentrated primarily in the eastern part of the basin. On average, the infiltration rate was concentrated in the middle of the basin, and it significantly decreased in the western parts of the basin, which represent the water division areas and sources of the basin.

The study examines groundwater recharge in the AS SAHBAA basin, which contains 126 sub-basins. The infiltration volume was measured using three methodologies: Tonder and Kirchner (1991), Singh (1973), and Chandra and Saxena (1975), each yielding varying results based on basin area and infiltration rates.

Using the Tonder and Kirchner method, average groundwater recharge was calculated between 0.1 million m^3 and 4.3 million m^3, with maximum infiltration rates resulting in recharge figures ranging from 2.45 million m^3 to 11.42 million m^3. Conversely, the Singh method indicated a higher average recharge of 12.43 million m^3, with a range from 4.4 million m^3 to 25.7 million m^3. When applying the maximum infiltration rate of 31.68 mm, the highest recharge levels were found between 12 million m^3 and 60.84 million m^3.

The Chandra and Saxena method yielded the most substantial average groundwater recharge figures, averaging 38.27 million m^3 with values ranging from 22.5 million m^3 to 57.3 million m^3. Utilizing the maximum calculated infiltration rate with this method, the recharge could potentially reach as high as 528.13 million m^3 to 1341.86 million m^3.

Visual representation in Figure 12 highlights that the northern and western sub-basins exhibit the highest recharge volumes, attributed to their larger area compared to other sub-basins in the study area. Overall, the variability in groundwater recharge across the sub-basins underscores the importance of method selection and basin configuration in hydrological assessments.

Table 3. Estimated Groundwater Recharge Rates (mm) and Volume (million m^3) in Wadi AS SAHBAA (2013–2022).

Years	Tonder and Kirchner 1991							Singh 1973							Chandra and Saxena 1975						
	Max.		Min.		Mean			Max.		Min.		Mean			Max.		Min.		Mean		
	(mm)	Million m^3	(mm)	Million m^3	(mm)	(%) of Rain	Million m^3	(mm)	Million m^3	(mm)	Million m^3	(mm)	(%) of Rain	Million m^3	(mm)	Million m^3	(mm)	Million m^3	(mm)	(%) of Rain	Million m^3
2013	6.62	43.81	0.04	0.033	1.79	1.24	1.8	36.84	309.83	2.28	0.236	12.66	9.7	13.2	67.45	1044.51	3.09	0.79	42.68	29.9	44.8
2014	3.67	17.87	0	0.014	0.73	0.64	0.8	22.08	180.37	0.12	0.137	7.37	8.5	7.7	52.31	735.91	1.89	0.56	30.07	25.6	31.4
2015	5.93	31.08	0.08	0.024	1.27	1.03	1.3	33.36	259.41	2.04	0.197	10.05	9.3	11.07	63.94	919.94	5.04	0.7	37.59	29.6	39.3
2016	5.23	35	0.02	0.027	1.43	1.36	1.5	29.88	319.37	3.84	0.242	13.05	10	13.6	60.23	893.27	13.57	0.679	36.5	30.2	38.1
2017	4.66	27.41	0.01	0.021	1.12	0.92	1.2	27	228.09	0.6	0.173	9.32	9.1	9.7	59.62	771.88	8.04	0.587	31.54	28.9	32.9
2018	9.38	86.88	0.05	0.066	3.55	1.69	3.7	50.64	525.68	3.96	0.399	21.48	10.6	22.4	79.83	1195.51	14.14	0.909	48.85	30.3	51
2019	11.42	102.3	0.43	0.078	4.18	1.78	4.3	60.84	602.53	5.88	0.458	24.62	10.8	25.7	87.88	1341.86	21.31	1.02	54.83	30.4	57.3
2020	4.06	23.49	0	0.018	0.96	0.89	1	24	208.76	0.12	0.159	8.53	9.1	8.9	53.39	773.1	9.43	0.588	31.59	28.7	33
2021	1.66	2.45	0	0.002	0.1	0.07	0.1	12	102.79	0	0.078	4.2	7.2	4.4	30.76	528.13	5.04	0.402	21.58	24.6	22.5
2022	3.29	17.87	0	0.014	0.73	0.7	0.8	20.16	179.87	0	0.137	7.35	8.7	7.7	48.4	760.13	10.98	0.58	31.06	27.2	32.4
Ave.	5.59	38.82	0.06	0.03	1.59	1.03	1.65	31.68	291.67	1.88	0.22	11.86	9.3	12.43	60.38	896.42	9.25	0.68	36.63	28.54	38.27

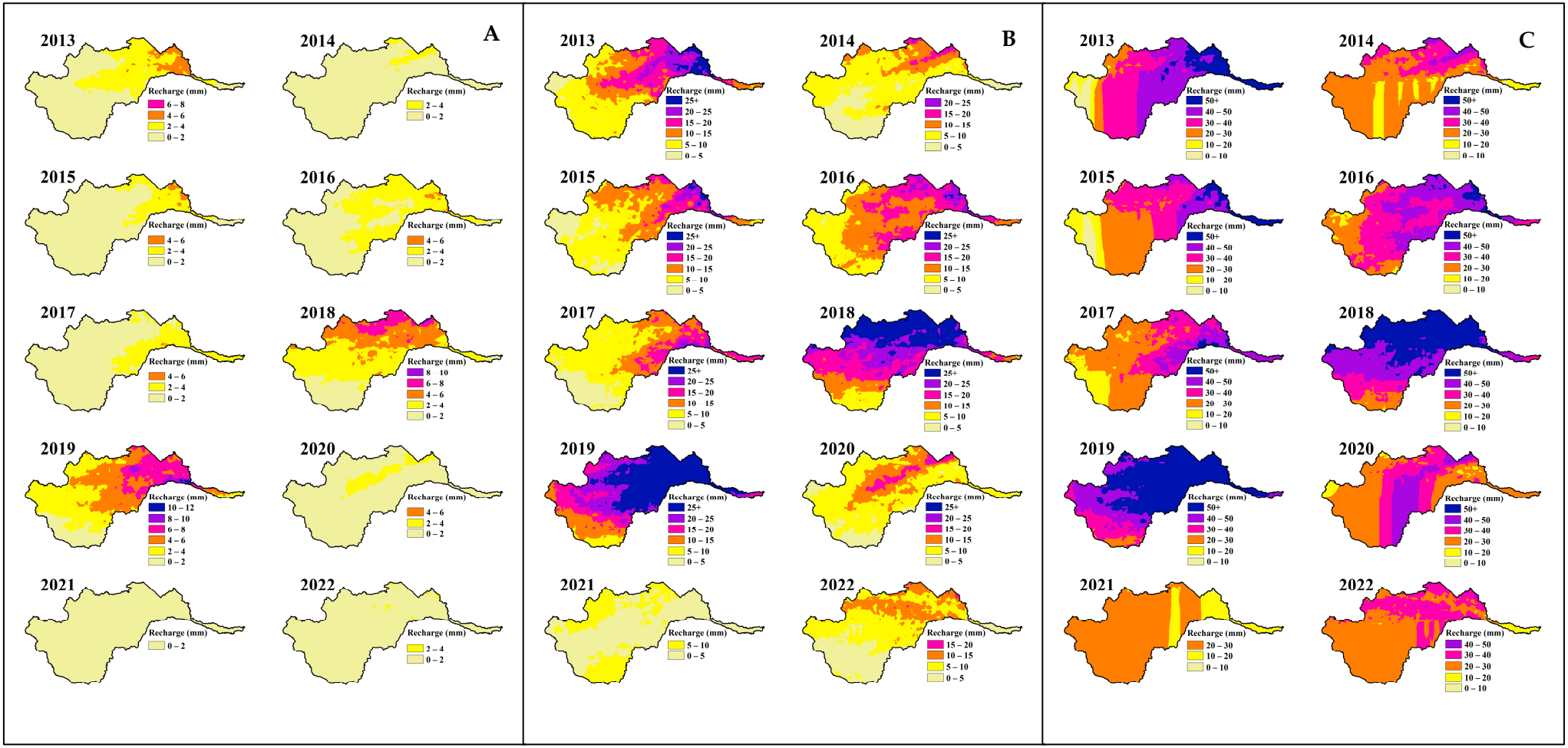


Figure 11. Spatio-Temporal Changes in Groundwater Recharge Rates in Wadi AS SAHBAA (2013–2022), (**A**) is Tonder and Kirchner (1991), (**B**) is the Singh (1973), and (**C**) is the Chandra and Saxena (1975) method.

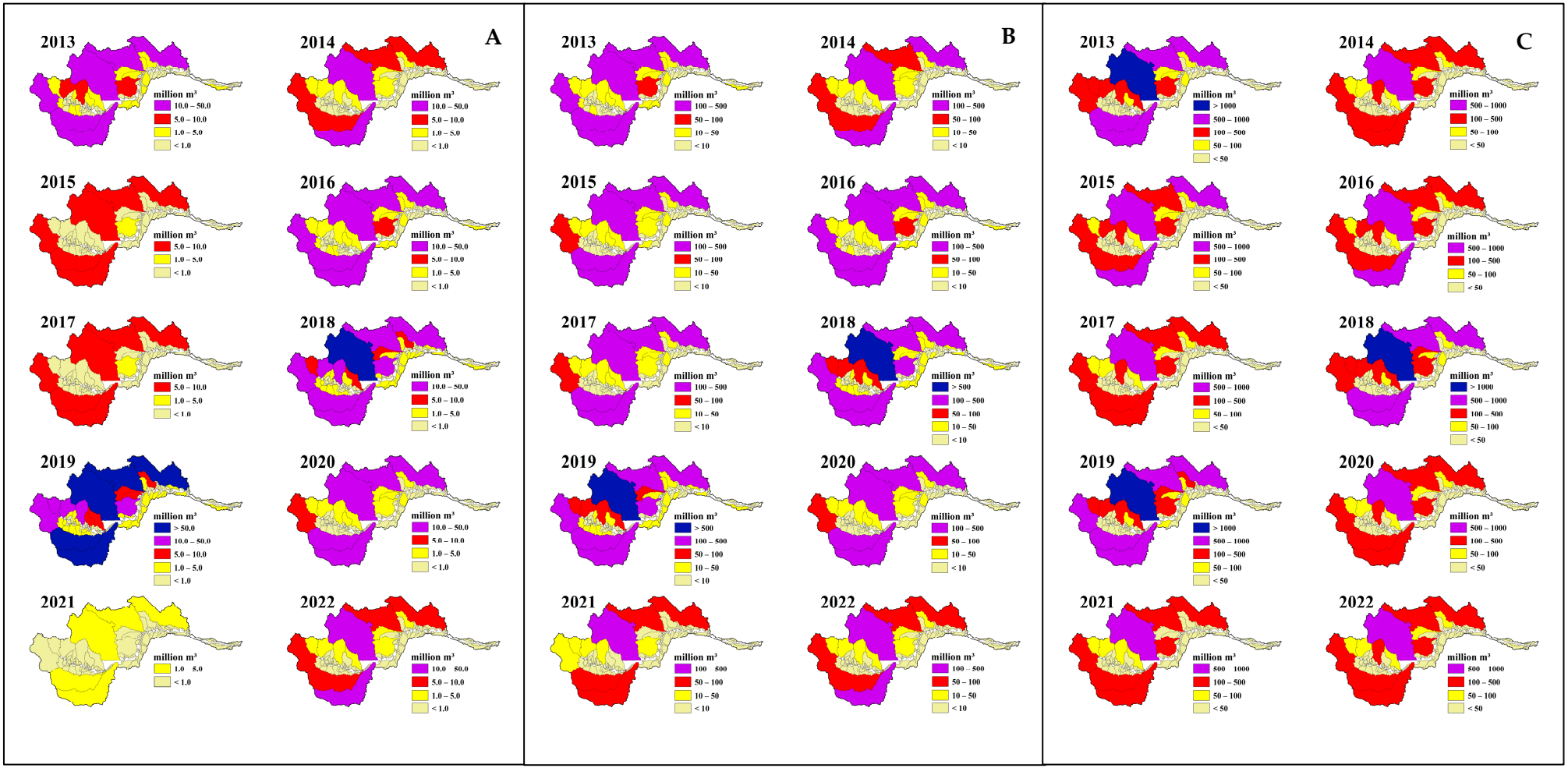


Figure 12. Spatio-Temporal Changes in Groundwater Recharge Rates in Wadi AS SAHBAA sub-basins (2013–2022), (**A**) is Tonder and Kirchner (1991), (**B**) is the Singh (1973), and (**C**) is the Chandra and Saxena (1975) method.

https://doi.org/10.3390/w18162023

The leakage during the lag time method is a useful approach for calculating groundwater recharge volumes by considering specific components of drainage basins and the impact of surface sediments. The average recharge volume determined through this method is 2.39 million m^3, with a notable range from 348 million m^3 to 81.61 million m^3, indicating significant variability among different sub-basins (Figure 12). According to the findings, 11 sub-basins exhibit annual recharge volumes below 1000 m^3, while 32 sub-basins have recharge volumes from 1000 to 5000 m^3. Additionally, 35 sub-basins recharge between 5000 and 25,000 m^3, and 32 sub-basins show recharge volumes ranging from 25,000 to 500,000 m^3. Furthermore, there are 16 sub-basins that exceed a recharge volume of 500,000 m^3 annually, highlighting diverse hydrogeological conditions within the study area. The total volume of groundwater recharge using this method is 301.07 million m^3.

Using the seepage or leakage during discharge time method, which incorporates specific factors related to drainage basins, the study assessed groundwater recharge volumes. Key elements considered included rock type, basin discharge time, elevation, and the number of channels. The analysis revealed that the average groundwater recharge volume across the studied basins is 1.42 million m^3, with significant variability, as the values range from a minimum of 1137 m^3 to a maximum of 47.04 million m^3 (Figure 13). The distribution of recharge volumes among the basins is noteworthy: approximately 11 basins reported groundwater recharge volumes below 5000 m^3, while 60 basins exhibited recharge volumes between 5000 m^3 and 500,000 m^3. Additionally, 26 basins manifested recharge volumes ranging from 50,000 m^3 to 500,000 m^3, and an impressive 17 basins surpassed an annual recharge volume of 500,000 m^3. This comprehensive overview emphasizes the diversity in groundwater recharge across different basins, reflecting variations in environmental and geological characteristics. The total volume of groundwater recharge using this method is 178.62 million m^3.

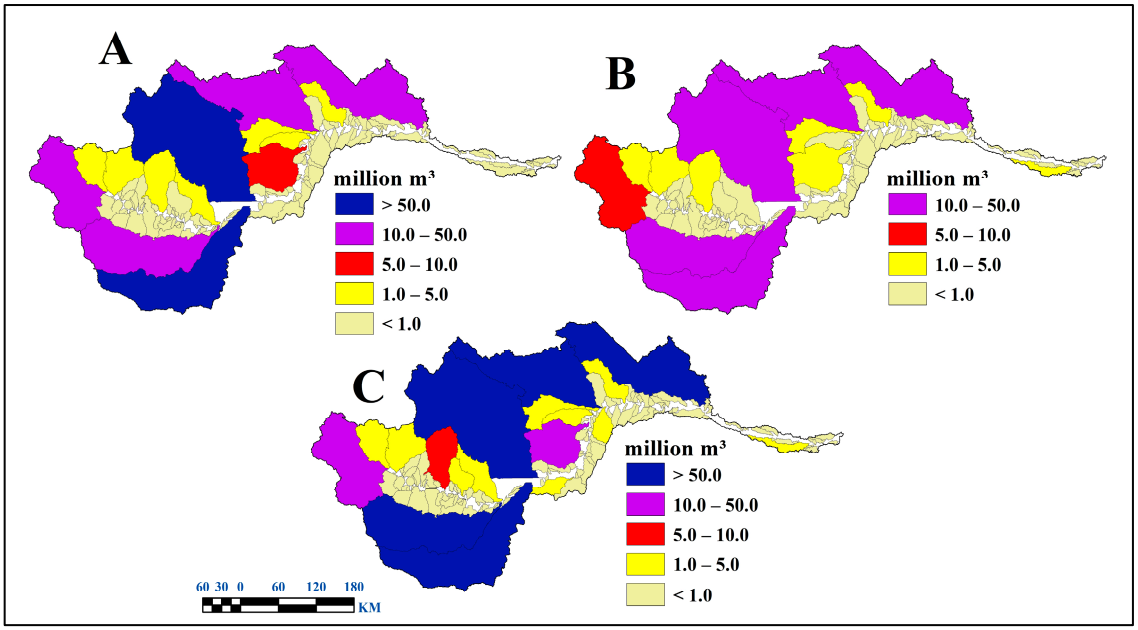


Figure 13. Infiltration in Wadi AS SAHBAA, (**A**) is leakage during the lag time method, (**B**) is seepage or leakage during discharge time method, and (**C**) is total basin infiltration method.

Using the total basin infiltration equation, the estimated total volume of groundwater recharge was calculated through the leakage during the lag time and seepage methods. The findings reveal that the average volume of groundwater recharge is approximately 3.81 million m^3, with values fluctuating between 1523 m^3 and 128.65 million m^3 (Figure 12).

Furthermore, the annual total infiltration and groundwater recharge for the AS SAHBAA basin is reported to be around 479.7 million m^3.

4. Discussion

The study area categorized as an arid region exhibits mean annual precipitation of 9.7 mm, resulting in a total annual rainfall of 116.6 mm. The rainfall fluctuates significantly between years; during periods of heavy rain, it can increase to a mean annual precipitation of 18.5 mm in 2019, corresponding to a total of 222.3 mm of rainfall for that year. Conversely, during years characterized by low precipitation such as 2021, the mean annual precipitation drops to 4.5 mm with the total annual rainfall reduced to 53.8 mm. This variability highlights the region's susceptibility to fluctuations in precipitation, indicating a broader trend in the climate dynamics within arid zones. This is in agreement with [32], in which the mean of total precipitation during 1970–2012 ranged between 0.1 and 513.8 mm, with an average maximum rainfall of 51.75 mm and minimum rainfall of 0.36 mm. On the other hand, [37] found an average rainfall rate for Riyadh ranging between 4.9 and 9.9 mm during 1980–2017. In the study conducted by [8], it was observed that the total rainfall from 1985 to 2023 varied within the range of 49.68 mm to 209.5 mm. This range aligns well with the findings of the current research being discussed. Ref. [39] contradicted the current study by indicating increased rainfall in the Makkah region during 2022. Specifically, Jeddah received 182 mm of rain, Taif recorded 143.3 mm, and Al-Jumum noted 109 mm. In contrast, the central Saudi Arabia region experienced one of its driest years, with an average total rainfall of only 79.4 mm. The study suggests that varying location and topography may have played a significant role in the disparities observed in rainfall patterns between the Makkah region and central Saudi Arabia.

Precipitation is a primary water source, contributing indirectly to groundwater storage through infiltration into aquifers. Rainfall is seasonal; the highest amounts occur during winter and spring, while it decreases in autumn and is non-existent during the summer, which agrees with [22,32,42,49]. Rainfall is characterized by its sudden nature; Long dry spells are often followed by short, intense bursts of rain that can cause significant damage to life and property. Precipitation is influenced by local topography, land cover, atmospheric conditions, and regional climatic influences (such as pressure zones) that dictate the frequency of rainstorms, in accordance with the findings of [37]. There is a direct positive correlation between the number and intensity of rainstorms and the total volume of precipitation. This interpretation aligns with studies that discuss rainfall intensity and periodically in arid regions [35,36,75,77,78].

The amount of rainfall has fluctuated significantly during the study period due to changes in the number of rainy days, which varies from year to year due to the frequency and severity of rainstorms. Some years of the study period have an increase in the rain intensity, like years 2018–2022–2015–2016, which recorded increases of 104.9–47.6–28.4–25.1%, respectively, and recorded decreases including 35.7% in 2014, 24.6% in 2017, 59.6% in 2020, and 40.1% in 2021. This is consistent with observations from the Arabian Peninsula discussing the rain potential and changes in arid regions [8,76,79,84].

The study area has experienced a significant downward trend in rainfall during specific years, primarily driven by a decrease in the number of rainy days. This volatility is a direct result of changes in the frequency and volume of rainstorms passing through the region, which aligns with [6,8,38]. Spatial variations in expected rainfall within the study area indicate noteworthy concentrations, specifically in the northern and eastern regions during select years, while other years show significant rainfall patterns concentrated in the northern and western areas.

The study analyzed the impact of human activities on rainfall patterns in a specific region, particularly focusing on the years 2020 and 2021. During this period, the COVID-19 pandemic led to a significant reduction in human activities, which corresponded with a marked decrease in both the frequency and intensity of rainstorms in the area. The findings indicate that rainfall is predominantly concentrated in the northern part of the region, where the urban center of Riyadh is situated. This urban heat island effect plays a critical role in influencing the intensity of rainstorms, suggesting a complex interaction between human-induced environmental changes and natural weather patterns, which agree with [11].

Uncertainty in satellite-derived rainfall measurements can exhibit significant variability due to multiple factors, including the methodology used for data retrieval, the meteorological conditions, and wind speed variations. Consequently, it is essential to compare the bias present in the satellite data to enhance its accuracy. In this study, we utilized hourly rainfall data collected from environmental ground stations managed by the National Center of Meteorology to find the degree of correlation between satellite data and field data and set the significant of the satellite data. Because these data sets are directly measured at the surface, we thought that they would be far more dependable. The scale and resolution of this in situ observed rainfall data are different from that of the satellite rainfall since the latter is an estimation based on pixels, while the former is sparsely located and only provides point-scale observations. Nevertheless, several statistical characteristics were examined, and satellite rainfall was retrieved using the exact x and y coordinates of the observed rainfall data. It is suggested that a variable of interest, represented as (y), may be influenced by another variable, denoted as (x). An analysis of the data, illustrated through a scatter diagram correlating climatic station rainfall with satellite rainfall, indicates a linear relationship characterized by a significant coefficient of correlation (R^2 = 0.81), indicating a strong association between the two datasets, as summarized in Table 4. Additionally, Figure 14 shows a correlation coefficient of 0.658, further highlighting the moderate to strong relationship between field observations and satellite estimates. This is consistent with what was stated in the study [92].

Table 4. Comparison of Field-Measured and Satellite-Derived Rainfall in Wadi AS SAHBAA (2013–2022).

Years	Climate Stations Data	Satellite Data	Difference	std.
2013	84.902	122.8	−37.898	26.79
2014	82.902	78.9	4.002	2.83
2015	89.202	101.3	−12.098	8.55
2016	119.9	126.7	−6.8	4.81
2017	83.801	95.5	−11.699	8.27
2018	108.201	195.5	−87.299	61.73
2019	160.9	222.3	−61.4	43.42
2020	40.302	89.8	−49.498	35.00
2021	18.303	53.8	−35.497	25.10
2022	92.4	79.4	13	9.19
Ave.	88.0813	116.6	−28.5187	20.16

The study emphasizes the importance of comparing various PERSIANN data models, including PERSIANN CCS-CDR, against ground-based measurements recorded at the Riyadh weather station. Additionally, it suggests the need for calibrating PERSIANN

data with field-measured observations from multiple locations over designated time frames, aiming to enhance the comprehensiveness and broader applicability of the data obtained [50,56,59,92,93].

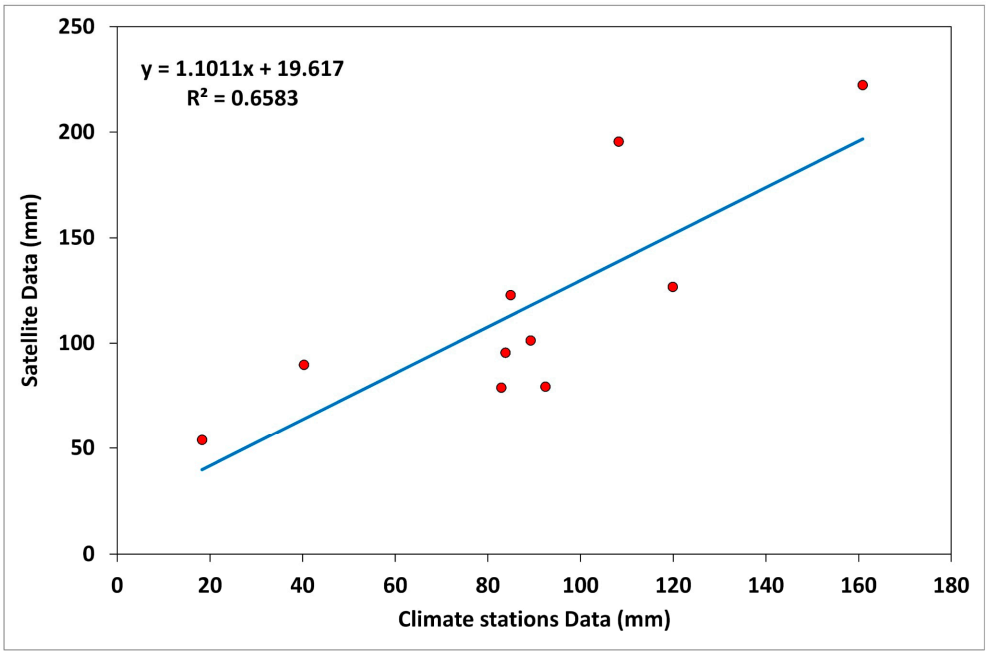


Figure 14. Correlation plot of observed rainfall data against satellite rainfall data for the period of 2013–2022.

Changes in the volume and distribution of rainwater infiltration into aquifers are influenced by a variety of factors. Key among these are spatial and temporal variations in rainfall, which affect both the quantity and timing of water that infiltrates into the ground. Additionally, geological and soil conditions play a significant role, as different types of soil and underlying rock can either enhance or restrict the movement of water [121].

The study concluded that the groundwater recharge rate ranged from 1.59 to 11.86 to 36.63 mm for the three methods used. The average groundwater recharge rate using the [122] method was 1.59 mm, representing 1.03% of the rainfall volume. This rate varied from year to year due to changes in rainfall volume. This rate was consistent with the [122] study, where the groundwater recharge rate ranged from 3% to 5% of the rainfall volume, with an average of 2.2%. However, the average recharge rate reached 12.8 mm due to the high rainfall volume, which ranged from 287 to 584 mm. Furthermore, this groundwater recharge percent of rainfall agrees with [64], which found that this rate ranged between 0.5 and 8.0% of rainfall, while [65] found that the percentage of groundwater recharge from rainwater ranges between 4 and 6% of the rainfall volume. Calculating the groundwater recharge rate using the [119] method yields an average of 11.86 mm, constituting 9.3% of the rainfall volume. This aligns with [120] study, which reported recharge rates between 24 and 198 mm yr−1, or 4.1 and 19.7% of the local average seasonal rainfall. Calculating groundwater recharge using the method of [121] shows an average rate of 36.63 mm or 54.28% of rainfall. This aligns with [114], where recharge rates varied between 9.92% and 12.40% of rainfall. By analyzing the outcomes of three distinct methodologies for calculating groundwater recharge, it is evident that the method proposed by Singh (1973) is the most effective for the study area in question. This conclusion is drawn from a comparative evaluation of the results derived from the various methods, establishing Singh's approach as superior to the others employed in this analysis.

Climatic factors, particularly evaporation rates, also impact this process by affecting how much water is available for infiltration. Together, these elements create a complex interplay that determines the effectiveness of rainwater infiltration into aquifers. Rainwater infiltration values typically exhibit a proportional distribution relative to precipitation levels; however, variations do occur due to shifts in geological and topographical factors. These factors influence how effectively rainwater penetrates the soil and underlying strata, thereby affecting overall water absorption rates and groundwater recharge. This interplay highlights the importance of considering local geological and topographical contexts when assessing rainwater infiltration dynamics. The calculation of groundwater recharge involves various techniques; due to the limitations of each approach, using multiple methods is recommended to improve estimates. These diverse approaches can complement each other and enhance the conceptual model of recharge processes.

5. Conclusions

This study employed satellite imagery and digital datasets to monitor cloud coverage, estimate precipitation, and assess groundwater recharge in the Wadi AS SAHBAA basin during 2013–2022. The precipitation estimation from remotely sensed information using artificial neural networks–cloud classification system–climate data record (PERSIANN-CCS-CDR) algorithm provided high-resolution estimates of rainfall, which were analyzed on annual, seasonal, and monthly scales. The study established a quantitative relationship between precipitation and groundwater recharge, demonstrating how rainfall infiltrates aquifers and contributes to the storage capacity of local groundwater reservoirs.

The results revealed significant temporal and spatial variability in precipitation, with annual precipitation of 116.6 mm/year and mean annual precipitation of 9.7 mm during the study period. Notable fluctuations occurred, including decreases of 35.7% in 2014, 24.6% in 2017, 59.6% in 2020, and 40.1% in 2021, reflecting both climatic variability and human impacts, such as the temporary reduction in activity during the COVID-19 pandemic. Rainfall was highly seasonal, concentrated in winter and spring, with minimal amounts in summer. Rain events were often sudden and intense, leading to flash floods and rapid surface runoff.

Groundwater recharge was estimated at an average ranging between 1.59 and 36.63 mm, representing 1.03–28.5% of rainfall. Recharge rates varied across the study years, influenced by rainfall intensity, duration, and spatial distribution, with the highest annual recharge observed in 2019 (1.78–30.4%). Satellite-derived rainfall data correlated strongly with field measurements (R^2 = 0.81), highlighting the value of remote sensing for hydrological studies while emphasizing the need for calibration with ground-based observations. The study also highlighted the importance of geological and geomorphological factors, such as fractured bedrock and sedimentary formations, in controlling infiltration and storage.

The findings of this study provide valuable guidance for sustainable water resource management and regional development in Wadi AS SAHBAA, as quantifying rainfall patterns and groundwater recharge offers critical insights for planning agricultural activities, urban water supply, and industrial development. Decision-makers can use these results to prioritize areas for groundwater protection, implement artificial recharge schemes, and optimize irrigation practices to reduce water waste. Moreover, the study demonstrates the potential of integrating satellite data with traditional field observations to establish a continuous monitoring system for precipitation and groundwater resources, an approach that can be scaled to other arid regions of the Arabian Peninsula, offering a model for evidence-based water management under climate change scenarios. By predicting areas of high recharge and identifying periods of low precipitation, water managers can allocate

resources more efficiently, reduce vulnerability to drought, and enhance resilience against extreme weather events. The study also underscores the importance of developing adaptive strategies for sustainable water use, including expanding meteorological and hydrological monitoring networks to improve calibration of satellite-derived data, implementing water-saving agricultural technologies such as drip irrigation and soil moisture monitoring, promoting artificial groundwater recharge in strategic locations to enhance aquifer storage, integrating urban planning with hydrological data to mitigate the urban heat island effect and prevent localized flooding, and conducting further research to refine predictive models for rainfall and recharge under changing climate conditions.

Despite these contributions, challenges remain. Sparse ground-based observations and uncertainties in satellite rainfall measurements introduce variability into water budgets. Human activities, including urbanization and intensive agriculture, increase pressure on limited groundwater reserves. Climate change is expected to exacerbate these challenges by altering precipitation patterns, evaporation rates, and recharge dynamics. Therefore, effective adaptation and policy strategies are essential to ensure the long-term sustainability of water resources.

In conclusion, this study not only provides a robust framework for monitoring precipitation and groundwater recharge in Wadi AS SAHBAA but also contributes practical recommendations for regional development and sustainable water management. The integration of satellite remote sensing, hydrogeological analysis, and field measurements presents a comprehensive tool to support decision-making, mitigate the impacts of climate variability, and promote resilience in water-scarce regions.

Author Contributions: Conceptualization, H.M. and M.A.A.; methodology, H.M. and M.A.A.; software, H.M. and M.A.A.; validation, H.M.; formal analysis, H.M. and M.A.A.; investigation, H.M., M.A.-M., E.H., H.A., A.S. and M.A.A.; resources, H.M., M.A.-M. and A.A.-B.; data curation, H.M., A.S. and M.A.A.; writing—original draft preparation, H.M., A.A.-B., M.A.A., M.A.-M., E.H., A.S. and H.A.; writing—review and editing, H.M., A.A.-B., M.A.-M., E.H. and H.A.; visualization, M.A.A.; supervision, H.M.; project administration, H.M.; funding acquisition, A.A.-B. and M.A.-M. All authors have read and agreed to the published version of the manuscript.

Funding: This research was funded by Princess Nourah bint Abdulrahman University Researchers Supporting Project number (PNURSP2026R241), Princess Nourah bint Abdulrahman University, Riyadh, Saudi Arabia.

Data Availability Statement: The original contributions presented in this study are included in the article. Further inquiries can be directed to the corresponding authors.

Acknowledgments: Princess Nourah bint Abdulrahman University Researchers Supporting Project number (PNURSP2026R241), Princess Nourah bint Abdulrahman University, Riyadh, Saudi Arabia. The authors explicitly states that generative artificial intelligence (AI) and AI-assisted technologies were used solely for language editing and proofreading of the manuscript and not for the content, analysis, or interpretation of the research.

Conflicts of Interest: M.A.A. is employed by Enshaat Al-Sayer General Trading and Contracting Company. The remaining authors declare that the research was conducted in the absence of any commercial or financial relationships that could be construed as a potential conflict of interest.

Abbreviations

COVID-19	Coronavirus Disease 2019
KSA	Kingdom of Saudi Arabia
TRMM	Tropical Rainfall Measuring Mission
GPM	Global Precipitation Measurement

PERSIANN-CDR	Precipitation Estimation from Remotely Sensed Information using Artificial Neural Networks–Climate Data Record
GPCP	Global Precipitation Climatology Project
CPC	Climate Prediction Center
PERSIANN-CCS	Precipitation Estimation from Remotely Sensed Information using Artificial Neural Networks–Cloud Classification System
SOFM	Self-Organizing Feature Map
IMERG	Integrated Multi-satellite Retrievals for GPM
CHRS	Center for Hydrometeorology and Remote Sensing
DEM	Digital Elevation Model
SAR	Synthetic Aperture Radar
SRTM	Shuttle Radar Topography Mission
NASA	National Aeronautics and Space Administration
NOAA	National Oceanic and Atmospheric Administration
TanDEM-X	TerraSAR-X add-on for Digital Elevation Measurement
TerraSAR-X	Terra Synthetic Aperture Radar-X

References

1. Faid, A.M.; El Zawahry, M.K.; Nasr, A. Surface and subsurface factors controlling groundwater recharge in Kom Ombo, Nile Valley. In *Proceedings of the 13th Symposium of Phanerozoic & Development in Egypt*; Al-Azhar University: Cairo, Egypt, 2003; pp. 61–77.
2. Ayenew, T. Numerical Groundwater Flow Modeling of the Central Main Ethiopian Rift Lakes Basin. *SINET Ethiop. J. Sci.* **2001**, *24*, 167–184. [CrossRef]
3. Yu, Z.; Yang, K.; Luo, Y.; Shang, C. Spatial-Temporal Process Simulation and Prediction of Chlorophyll-a Concentration in Dianchi Lake Based on Wavelet Analysis and Long-Short Term Memory Network. *J. Hydrol.* **2020**, *582*, 124488. [CrossRef]
4. Koch, M.; Missimer, T.M. Water Resources Assessment and Management in Drylands. *Water* **2016**, *8*, 239. [CrossRef]
5. Amparo-Salcedo, M.; Pérez-Gimeno, A.; Navarro-Pedreño, J. Water Security Under Climate Change: Challenges and Solutions Across 43 Countries. *Water* **2025**, *17*, 633. [CrossRef]
6. Alghamdi, A.G.; Aly, A.A.; Majrashi, M.A.; Ibrahim, H.M. Impact of climate change on hydrochemical properties and quality of groundwater for domestic and irrigation purposes in arid environment: A case study of Al-Baha region, Saudi Arabia. *Environ. Earth Sci.* **2023**, *82*, 39. [CrossRef]
7. Mushtaq, F.; Rehman, H.; Ali, U.; Babar, M.S.; Al-Suwaiyan, M.S.; Yaseen, Z.M. An investigation of recharging groundwater levels through river ponding: New strategy for water Management in Sutlej River. *Sustainability* **2023**, *15*, 1047. [CrossRef]
8. Munir, S.; Habeebullah, T.M.A.; Zamreeq, A.O.; Alfehaid, M.M.A.; Ismail, M.; Khalil, A.A.; Baligh, A.A.; Islam, M.N.; Jamaladdin, S.; Ghulam, A.S. Understanding Changing Trends in Extreme Rainfall in Saudi Arabia: Trend Detection and Automated EVT-Based Threshold Estimation. *Climate* **2025**, *13*, 233. [CrossRef]
9. Tooth, S. Process, form and change in dryland rivers: A review of recent research. *Earth Sci. Rev.* **2000**, *51*, 67–107. [CrossRef]
10. Wade, A.J.; Smith, S.J.; Black, E.C.L.; Brayshaw, D.J.; Holmes, P.A.C.; El-Bastawesy, M.; Rambeau, C.M.C.; Mithen, S.J. A new method for the determination of Holocene palaeohydrology. *J. Hydrol.* **2012**, *420*, 1–16. [CrossRef]
11. Steensen, B.M.; Marelle, L.; Hodnebrog, Ø.; Myhre, G. Future urban heat island influence on precipitation. *Clim. Dyn.* **2022**, *58*, 3393–3403. [CrossRef]
12. El Bastawesy, M.; White, K.H.; Nassr, A.H. Integration of remote sensing and GIS for modeling flash floods in Wadi Hudain catchment. *Egypt Hydrol. Process.* **2009**, *23*, 1359–1368. [CrossRef]
13. Ntona, M.M.; Busico, G.; Mastrocicco, M.; Kazakis, N. Modeling groundwater and surface water interaction: An overview of current status and future challenges. *Sci. Total Environ.* **2022**, *846*, 157355. [CrossRef] [PubMed]
14. Khan, S.I.; Hong, Y.; Wang, J.; Yilmaz, K.K.; Gourley, J.J.; Adler, R.F.; Brak Enridge, G.R.; Policelli, F.; HabibIrwin, S.D. Satellite remote sensing and hydrologic modeling for flood inundation mapping in Lake Victoria basin: Implications for hydrologic prediction in ungauged basins. *IEEE Trans. Geosci. Remote Sens.* **2010**, *49*, 85–95. [CrossRef]
15. Swain, D.L.; Singh, D.; Touma, D.; Diffenbaugh, N.S. Attributing extreme events to climate change: A new frontier in a warming world. *One Earth* **2020**, *2*, 522–527. [CrossRef]
16. Seyyedi, H.; Anagnostou, E.N.; Beighley, E.; McCollum, J. Satellite-driven downscaling of global reanalysis precipitation products for hydrological applications. *Hydrol. Earth Syst. Sci.* **2014**, *18*, 5077–5091. [CrossRef]

17. Awais, M.; Li, W.; Cheema, M.J.M.; Hussain, S.; AlGarni, T.S.; Liu, C.; Ali, A. Remotely sensed identification of canopy characteristics using UAV-based imagery under unstable environmental condi tions. *Environ. Technol. Innov.* **2021**, *22*, 101465. [CrossRef]
18. Ricciardelli, E.; Di Paola, F.; Gentile, S.; Cersosimo, A.; Cimini, D.; Gallucci, D.; Geraldi, E.; Larosa, S.; Nilo, S.T.; Ripepi, E. Analysis of Livorno heavy rainfall event: Examples of satellite-based observation techniques in support of numerical weather prediction. *Remote Sens.* **2018**, *10*, 1549. [CrossRef]
19. Lu, D.; Yong, B. Evaluation and hydrological utility of the latest GPM IMERG V5 and GSMaP V7 precipitation products over the Tibetan Plateau. *Remote Sens.* **2018**, *10*, 2022. [CrossRef]
20. Tapiador, F.; Navarro, A.; Levizzani, V.; García-Ortega, E.; Huffman, G.; Kidd, C.; Kucera, P.; Kummerow, C.; Masunaga, H.; Petersen, W. Global precipitation measurements for validating climate models. *Atmos. Res.* **2017**, *197*, 1–20. [CrossRef]
21. Moazami, S.; Golian, S.; Kavianpour, M.R.; Hong, Y. Comparison of PERSIANN and V7 TRMM Multi-satellite Precipitation Analysis (TMPA) products with rain gauge data over Iran. *Int. J. Remote Sens.* **2013**, *34*, 8156–8171. [CrossRef]
22. Dasari, H.P.; Desamsetti, S.; Langodan, S.; Attada, R.; Ashok, K.; Hoteit, I. Long-term changes in the Arabian Peninsula rainfall and their relationship with the ENSO signals in the tropical Indo-Pacific. *Clim. Dyn.* **2021**, *59*, 1715–1731. [CrossRef]
23. Trenberth, K.E.; Dai, A.; Rasmussen, R.M.; Parsons, D.B. The changing character of precipitation. *Bull. Am. Meteorol. Soc.* **2003**, *84*, 1205–1218. [CrossRef]
24. Wang, B.; Liu, J.; Kim, H.-J.; Webster, P.J.; Yim, S.-Y. Recent change of the global monsoon precipitation (1979–2008). *Clim. Dyn.* **2012**, *39*, 1123–1135. [CrossRef]
25. Miao, Q.; Pan, B.; Wang, H.; Hsu, K.; Sorooshian, S. Improving Monsoon Precipitation Prediction Using Combined Convolutional and Long Short Term Memory Neural Network. *Water* **2019**, *11*, 977. [CrossRef]
26. Behrangi, A.; Khakbaz, B.; Jaw, T.C.; AghaKouchak, A.; Hsu, K.; Sorooshian, S. Hydrologic evaluation of satellite precipi tation products over a mid-size basin. *J. Hydrol.* **2011**, *397*, 225–237. [CrossRef]
27. Su, F.; Gao, H.; Huffman, G.J.; Lettenmaier, D.P. Potential utility of the real-time TMPA-RT precipitation estimates in streamflow prediction. *J. Hydrometeorol.* **2011**, *12*, 444–455. [CrossRef]
28. Jiang, S.; Ren, L.; Hong, Y.; Yong, B.; Yang, X.; Yuan, F.; Ma, M. Comprehensive evaluation of multi-satellite precipitation prod ucts with a dense rain gauge network and optimally merging their simulated hydrological flows using the Bayesian model averaging method. *J. Hydrol.* **2012**, *452*, 213–225. [CrossRef]
29. Bahrawi, J.; Alqarawy, A.; Chabaani, A.; Elfeki, A.; Elhag, M. Spatiotemporal analysis of the annual rainfall in the Kingdom of Saudi Arabia: Predictions to 2030 with different confidence levels. *Theor. Appl. Climatol.* **2021**, *146*, 1479–1499. [CrossRef]
30. Artan, G.; Gadain, H.; Smith, J.L.; Asante, K.; Bandaragoda, C.J.; Verdin, J.P. Adequacy of satellite derived rainfall data for stream flow modeling. *Nat. Hazards* **2007**, *43*, 167–185. [CrossRef]
31. Alharthi, A.; El-Sheikh, M.A.; Elhag, M.; Alatar, A.A.; Abbadi, G.A.; Abdel Salam, E.M.; Arif, I.A.; Baeshen, A.A.; Eid, E.M. Remote sens ing of 10 years changes in the vegetation cover of the northwest ern coastal land of Red Sea, Saudi Arabia. *Saudi J. Biosoc. Sci.* **2020**, *27*, 3169–3179.
32. Elfeki, A.; Bahrawi, J.; Latif, M.; Hannachi, A. Spatiotemporal analysis of monthly rainfall over Saudi Arabia and global teleconnections. *Geomat. Nat. Hazards Risk* **2022**, *13*, 2618–2648. [CrossRef]
33. Gu, H.-H.; Yu, Z.-B.; Yang, C.-G.; Ju, Q.; Lu, B.-H.; Liang, C. Hydrologi cal assessment of TRMM rainfall data over Yangtze River Basin. *Water Sci. Eng.* **2010**, *3*, 418–430.
34. Camberlin, P.; Barraud, G.; Bigot, S.; Dewitte, O.; Makanzu Imwangana, F.; Maki Mateso, J.C.; Martiny, N.; Monsieurs, E.; Moron, V.; Pellarin, T. Evaluation of remotely sensed rainfall products over Central Africa. *Q. J. R. Meteorol. Soc.* **2019**, *145*, 2115–2138. [CrossRef]
35. Habib, E.; Nasrollahi, N. Evaluation of TRMM-TMPA Satellite Rainfall Estimates Over Arid Regions. In *Proceedings of the AGU Fall Meeting 2009*; AGUFM: San Francisco, CA, USA, 2009; p. H12A-02.
36. Farran, M.M.; Elfeki, A.; Elhag, M.; Chaabani, A. A comparative study of the estimation methods for NRCS curve number of natu ral arid basins and the impact on flash flood predications. *Arab. J. Geosci.* **2021**, *14*, 121. [CrossRef]
37. Luong, T.M.; Dasari, H.P.; Doan, Q.-V.; Alduwais, A.K.; Hoteit, I. Organized precipitation and associated large-scale circulation patterns over the Kingdom of Saudi Arabia. *Int. J. Climatol.* **2024**, *44*, 3295–3314. [CrossRef]
38. Almazroui, M. Rainfall Trends and Extremes in Saudi Arabia in Recent Decades. *Atmosphere* **2020**, *11*, 964. [CrossRef]
39. Zamreeg, A.O.; Islam, M.N.; Al-Azemi, M.A.; Alboogmy, S.Z.; Habeebullah, T.M.; Ghulam, A.S. Heavy and extreme rainfall in Makkah Region of Saudi Arabia at the present climate. *Discov. Sustain.* **2025**, *6*, 690. [CrossRef]
40. Maggioni, V.; Meyers, P.C.; Robinson, M.D. A review of merged high-resolution satellite precipitation product accuracy during the Tropical Rainfall Measuring Mission (TRMM) era. *J. Hydrometeorol.* **2016**, *17*, 1101–1117. [CrossRef]
41. Sun, Q.; Miao, C.; Duan, Q.; Ashouri, H.; Sorooshian, S.; Hsu, K.-L. A review of global precipitation data sets: Data sources, estimation, and intercomparisons. *Rev. Geophys.* **2018**, *56*, 79–107. [CrossRef]

42. Attada, R.; Dasari, H.P.; Kunchala, R.K.; Langodan, S.; Kondapalli, N.K.; Knio, O.; Hoteit, I. Evaluating cumulus param eterization schemes for the simulation of Arabian Peninsula winter rainfall. *J. Hydrometeorol.* **2020**, *21*, 1089–1114. [CrossRef]
43. Lobligeois, F.; Andréassian, V.; Perrin, C.; Tabary, P.; Loumagne, C. When does higher spatial resolution rainfall information improve streamflow simulation? An evaluation using 3620 flood events. *Hydrol. Earth Syst. Sci.* **2014**, *18*, 575–594. [CrossRef]
44. Vieux, B.E.; Imgarten, J.M. On the scale-dependent propagation of hydrologic uncertainty using high-resolution X-band radar rainfall estimates. *Atmos. Res.* **2012**, *103*, 96–105. [CrossRef]
45. Huang, Y.; Bárdossy, A.; Zhang, K. Sensitivity of hydrological models to temporal and spatial resolutions of rainfall data. *Hydrol. Earth Syst. Sci.* **2019**, *23*, 2647–2663. [CrossRef]
46. Cristiano, E.; Ten Veldhuis, M.; van de Giesen, N. Spatial and temporal variability of rainfall and their effects on hydrological response in urban areas-a review. *Hydrol. Earth Syst. Sci.* **2017**, *21*, 3859–3878. [CrossRef]
47. Ficchì, A.; Perrin, C.; Andréassian, V. Impact of temporal resolution of inputs on hydrological model performance: An analysis based on 2400 flood events. *J. Hydrol.* **2016**, *538*, 454–470. [CrossRef]
48. Lee, M.; Im, E.; Bae, D. Impact of the spatial variability of daily precipitation on hydrological projections: A comparison of GCM and RCM-driven cases in the Han River basin, Korea. *Hydrol. Process.* **2019**, *33*, 2240–2257. [CrossRef]
49. El Kenawy, A.M.; McCabe, M.F. A multi-decadal assess ment of the performance of gauge- and model-based rainfall products over Saudi Arabia: Climatology, anomalies and trends. *Int. J. Climatol.* **2016**, *36*, 656–674. [CrossRef]
50. Hsu, K.; Gao, X.; Sorooshian, S.; Gupta, H.V. Precipitation estimation from remotely sensed information using artificial neural networks. *J. Appl. Meteorol. Clim.* **1997**, *36*, 1176–1190. [CrossRef]
51. Meisner, B.N.; Arkin, P.A. Spatial and annual variation in the diurnal cycle of large-scale tropical convective cloudiness and precipitation. *Mon. Weather Rev.* **1987**, *115*, 1009–1032. [CrossRef]
52. Scofield, R.A. The NESDIS operational convective precipitation technique. *Mon. Weather Rev.* **1987**, *115*, 1773–1792. [CrossRef]
53. Kummerow, C.; Barnes, W.; Kozu, T.; Shiue, J.; Simpson, J. The Tropical Rainfall Measuring Mission (TRMM) sensor package. *J. Atmos. Ocean. Technol.* **1998**, *15*, 809–817. [CrossRef]
54. Kummerow, C.; Simpson, J.; Thiele, O.; Barnes, W.; Chang, A.T.C.; Stocker, E.; Adler, R.F.; Hou, A.; Kakar, R.; Wentz, F.; et al. The status of the Tropical Rainfall Measuring Mission (TRMM) after two years in orbit. *J. Appl. Meteorol.* **2000**, *39*, 1965–1982. [CrossRef]
55. Hou, A.Y.; Kakar, R.K.; Neeck, S.; Azarbarzin, A.A.; Kummerow, C.D.; Kojima, M.; Oki, R.; Nakamura, K.; Iguchi, T. The Global Precipitation Measurement Mission. *Bull. Am. Meteorol. Soc.* **2014**, *95*, 701–722. [CrossRef]
56. Ashouri, H.; Hsu, K.L.; Sorooshian, S.; Braithwaite, D.K.; Knapp, K.R.; Cecil, D.; Nelson, B.R.; Prat, O.B. PERSIANN-CDR: Daily precipitation climate data record from multisatellite observations for hydrological and climate studies. *Bull. Am. Meteorol. Soc.* **2015**, *96*, 69–83. [CrossRef]
57. Knapp, K.R. Scientific data stewardship of International Satellite Cloud Climatology Project B1 global geostationary observations. *J. Appl. Remote Sens.* **2008**, *2*, 23548. [CrossRef]
58. Rossow, W.B.; Duenas, E.N. The international satellite cloud climatology project (ISCCP) web site: An online resource for research. *Bull. Am. Meteorol. Soc.* **2004**, *85*, 167–172.
59. Sadeghi, M.; Nguyen, P.; Hsu, K.-L.; Sorooshian, S.; Braithwaite, D.; Knapp, K.R. Evaluation of PERSIANN-CDR Constructed Using GPCP V2. 2 and V2. 3 and A Comparison with TRMM 3B42 V7 and CPC Unified Gauge-Based Analysis in Global Scale. *Remote Sens.* **2019**, *11*, 2755.
60. Mohamed, H.R. Evaluation of satellite-based rainfall estimates and application to monitor flash floods in Wadi Araba region western Suez Gulf. *Bull. Société Géographie d'Egypte* **2024**, *97*, 25–56. [CrossRef]
61. Karbalaee, N.; Hsu, K.; Sorooshian, S.; Braithwaite, D. Bias Adjustment of Infrared Rainfall Estimation Using Passive Microwave Satellite Rainfall Data. *J. Geophys. Res. Atmos.* **2017**, *122*, 3857–3876. [CrossRef]
62. Sanford, W. Recharge and groundwater models: An overview. *Hydrogeol. J.* **2002**, *10*, 110–120. [CrossRef]
63. Rushton, K.R.; Ward, C. The estimation of groundwater recharge. *J. Hydrol.* **1979**, *41*, 345–361. [CrossRef]
64. Nolte, A.; Eley, M.; Schöniger, M.; Gwapedza, D.; Tanner, J.; Mantel, S.K.; Scheihing, K. Hydrological modelling for assessing spatio-temporal groundwater recharge variations in the water-stressed Amathole Water Supply System, Eastern Cape, South Africa. *Hydrol. Process.* **2021**, *35*, e14264. [CrossRef]
65. Abiye, T. Synthesis on groundwater recharge in Southern Africa: A supporting tool for groundwater users. *Groundw. Sustain. Dev.* **2016**, *2*, 182–189. [CrossRef]
66. Andualem, T.G.; Demeke, G.G.; Ahmed, I.; Dar, M.A.; Yiebeltal, M. Groundwater recharge estimation using empirical methods from rainfall and streamflow records. *J. Hydrol. Reg. Stud.* **2021**, *37*, 100917. [CrossRef]
67. Olmsted, F.H.; Hely, A.G. *Relation Between Groundwater and Surface Water in Brandywine Creek Basin*; US Government Printing Office: Washington, DC, USA, 1962.
68. Zektser, I.S. *Laws of Formation of Groundwater Runoff Study*; Nedra: Moscow, Russia, 1977; pp. 1–173.

69. Niazi, A.; Bentley, L.R.; Hayashi, M. Estimation of spatial distribution of groundwater recharge from stream baseflow and groundwater chloride. *J. Hydrol.* **2017**, *546*, 380–392. [CrossRef]
70. Misstear, B.D.R.; Brown, L.; Johnston, P.M. Estimation of groundwater recharge in a major sand and gravel aquifer in Ireland using multiple approaches. *Hydrogeol. J.* **2009**, *17*, 693–706. [CrossRef]
71. Dzhamalov, R.G. *Ground-Water Flow of the Terek-Kuma Artesian Basin*; Nauka: Moscow, Russia, 1973.
72. Monir, M.M.; Akhter, S. Impacts of irrigated agricultural land expansion on groundwater security in Mithapukur Upazila, Bangladesh. *J. Environ. Sci. Health Sustain.* **2026**, *2*, 20–29. [CrossRef]
73. Rausch, R.; Dirks, H. A hydrogeological overview of the Upper Mega Aquifer System on the Arabian Platform. *Hydrogeol. J.* **2024**, *32*, 621–634. [CrossRef]
74. Al-Harbi, O.A.; Hussain, G.; Lafouza, O. Irrigation water quality evaluation of Al-Mendasah groundwater and drainage water, Al-Madenah Al-Monawarah region, Saudi Arabia. *Int. J. Soil Sci.* **2010**, *5*, 282–300. [CrossRef]
75. AlSubih, M.; Kumari, M.; Mallick, J.; Ramakrishnan, R.; Islam, S.; Singh, C.K. Time series trend analysis of rainfall in last five decades and its quantification in Aseer Region of Saudi Arabia. *Arab. J. Geosci.* **2021**, *14*, 519. [CrossRef]
76. Alotaibi, B.A.; Baig, M.B.; Najim, M.M.; Shah, A.A.; Alamri, Y.A. Water scarcity management to ensure food scarcity through sustainable water resources management in Saudi Arabia. *Sustainability* **2023**, *15*, 10648. [CrossRef]
77. El-Rawy, M.; Fathi, H.; Zijl, W.; Alshehri, F.; Almadani, S.; Zaidi, F.K.; Aldawsri, M.; Gabr, M.E. Potential effects of climate change on agricultural water resources in Riyadh region, Saudi Arabia. *Sustainability* **2023**, *15*, 9513. [CrossRef]
78. Khan, M.Y.A.; ElKashouty, M.; Bob, M. Impact of rapid urbanization and tourism on the groundwater quality in Al Madinah city, Saudi Arabia: A monitoring and modeling approach. *Arab. J. Geosci.* **2020**, *13*, 922. [CrossRef]
79. Fazel, H.K.; Abdo, S.M.; Althaqafi, A.; Eldosari, S.H.; Zhu, B.-K.; Safaa, H.M. View of Saudi Arabia strategy for water resources management at Bishah, Aseer Southern Region. *Water Assess. Sustain.* **2022**, *14*, 4198. [CrossRef]
80. Ali, I.; Hasan, M.A.; Alharbi, O.M.L. Toxic metal ions contamination in the groundwater, Kingdom of Saudi Arabia. *J. Taibah Univ. Sci.* **2020**, *14*, 1571–1579. [CrossRef]
81. Al-Omran, A.M.; Aly, A.A.; Al-Wabel, M.I.; Sallam, A.S.; Al-Shayaa, M.S. Hydrochemical characterization of groundwater under agricultural land in arid environment: A case study of Al-Kharj, Saudi Arabia. *Arab. J. Geosci.* **2016**, *201*, 68. [CrossRef]
82. MEWA. *National Water Strategy 2030 (Arabic Language)*; Ministry of Environment, Water and Agriculture: Riyadh, Saudi Arabia, 2018.
83. Sharma, S.K. A novel approach on water resource management with multi-criteria optimization and intelligent water demand forecasting in Saudi Arabia. *Environ. Res.* **2022**, *208*, 112578. [CrossRef] [PubMed]
84. Abdelkareem, M.; Abdalla, F. Revealing potential areas of water resources using integrated remote-sensing data and GIS-based analytical hierarchy process. *Geocarto Int.* **2022**, *37*, 8672–8696. [CrossRef]
85. SWPC. *Seven-Year Statement for KSA's Water (Arabic Language)*; Ministry of Environment Water & Agriculture: Riyadh, Saudi Arabia, 2020.
86. Al-Qasimi. *The Gulf in Historic Maps 1478–1861*, 2nd ed.; H.H. Sultan bin Muhammad al-Qasimi: Sharjah, United Arab Emirates, 1999.
87. Al Shaikh, N.Y.; Claire, R. The "River Aftan": An old caravan/trade route along Wādī al-SahbāM? In Proceedings of the Seminar for Arabian Studies, London, UK, 23–25 July 2010; pp. 321–335.
88. Al Sayari, S.S.; Zotl, J.G. *Quaternary Period in Saudi Arabia 1. Sedimentological, Hydrogeological, Hydrochemical, Geomorphological, and Climatological Investigations in Central and Eastern Saudi Arabia*; Springer: Vienna, Austria, 1978. [CrossRef]
89. Steineke, M.; Bramkamp, R.A. Jurassic Ammonites from Jebel Tuwaiq, Central Arabia. *Philos. Trans. R. Soc. London. Ser. B Biol. Sci.* **1952**, *236*, 241–314. [CrossRef]
90. Powers, R.W.; Ramirez, L.F.; Redmond, C.D.; Elberg, E.L. *Geology of the Arabian Peninsula: Sedimentary Geology of Saudi Arabia*; U.S. Geological Survey Professional Paper 560; U.S. Geological Survey: Washington, DC, USA, 1966; pp. D1–D147.
91. Center for Hydrometeorology and Remote Sensing (CHRS). *CHRS Data Portal*; University of California: Irvine, CA, USA, 2013–2022. Available online: https://chrsdata.eng.uci.edu/ (accessed on 22 March 2025).
92. Sadeghi, M.; Nguyen, P.; Naeini, M.R.; Hsu, K.; Braithwaite, D.; Sorooshian, S. PERSIANN-CCS-CDR, a 3-hourly 0.04° global precipitation climate data record for heavy precipitation studies. *Sci. Data* **2021**, *8*, 157. [CrossRef] [PubMed]
93. Nguyen, P.; Shearer, E.; Tran HOmbadi, M.; Hayatbini, N.; Palacios, T.; Huynh, P.; Braithwaite, D.; Updegraff, G.; Hsu, K. The CHRS Data Portal, an easily accessible public repository for PERSIANN global satellite precipitation data. *Sci. Data* **2019**, *6*, 180296. [CrossRef] [PubMed]
94. Sorooshian, S.; Hsu, K.; Gao, X.; Gupta, H.V.; Imam, B.; Braithwaite, D. Evaluation of PERSIANN system satellite-based estimates of tropical rainfall. *Bull. Am. Meteorol. Soc.* **2000**, *81*, 2035–2046. [CrossRef]
95. Schindler, K.; Papasaika-hanusch, H.; Schütz, S.; Baltsavias, E. Improving Wide-Area DEMs Through Data Fusion—Chances and Limits. *Photogramm. Week* **2011**, *11*, 159–170.
96. Wilson, J.P. *Environmental Applications of Digital Terrain Modelling*; John Wiley & Sons Inc.: New York, NY, USA, 2018; 360p.

97. Yang, L.; Meng, X.; Zhang, X. SRTM DEM and its application advances. *Int. J. Remote Sens.* **2011**, *32*, 3875–3896. [CrossRef]
98. Hassan, A.; Albanai, J.A.; Al-Ali, J.; Fayad, M.; Atalla, M.A.; Abdelkarim, A.; Badawy, H.D. Assessment of flash flood risks in the desert cities: A case study on Sabah Al-Ahmad City, Kuwait. *J. Water Clim. Change* **2024**, *15*, 5107–5127. [CrossRef]
99. Dubayah, R.; Blair, J.B.; Goetz, S.; Fatoyinbo, L.; Hansen, M.; Healey, S.; Hofton, M.; Hurtt, G.; Kellner, J.; Luthcke, S.; et al. The Global Ecosystem Dynamics Investigation: High-resolution laser ranging of the Earth's forests and topography. *Sci. Remote Sens.* **2020**, *1*, 100002. [CrossRef]
100. Elkhrachy, I. Vertical accuracy assessment for SRTM and ASTER Digital Elevation Models: A case study of Najran city, Saudi Arabia. *Ain Shams Eng. J.* **2018**, *9*, 1807–1817. [CrossRef]
101. Okolie, C.J.; Smit, J.L. A systematic review and meta-analysis of Digital elevation model (DEM) fusion: Pre-processing, methods and applications. *ISPRS J. Photogramm. Remote Sens.* **2022**, *188*, 1–29. [CrossRef]
102. Geological Survey (USGS). *Shuttle Radar Topography Mission (SRTM)*; U.S. Geological Survey: Reston, VA, USA, 2009. [CrossRef]
103. Shebl, A.; Atalla, M.; Csámer, Á. Vertical Accuracy Assessment of DEMs around Jabal Al-Shayeb Area, Egypt. *Intercont. Geoinf. Days* **2021**, *3*, 42–45.
104. Denis, V.; Yves-Michel, N.; Daniel, V.; Jean, B.; Sylvie, C.; Martine, B.; Jérémie, G.; Mohammed, H.; Moujahed, A. The Permian-Triassic Khuff Formation of central Saudi Arabia. *GeoArabia* **2005**, *10*, 77–134. [CrossRef]
105. Aref, L.; Abdulrahman, A.; Khalid, A.; Mostafa, M.K.; Abdulla, A. Characterization of the Permo-Triassic upper Khuff reservoir, central Saudi Arabia: An integrated core plugs, petro-fabrics and mercury injection analysis. *J. Afr. Earth Sci.* **2018**, *145*, 284–296. [CrossRef]
106. Jaju, M.; Nader, F.H.; Roure, F.; Matenco, L. Optimal Aquifers and Reservoirs for CCS and EOR in the Kingdom of Saudi Arabia: An Overview. In *Lithosphere Dynamics and Sedimentary Basins of the Arabian Plate and Surrounding Areas. Frontiers in Earth Sciences*; Roure, F., Amin, A., Khomsi, S., Al Garni, M., Eds.; Springer: Cham, Switzerland, 2017.
107. Galluccio, L.; Al-Sinawi, N.; Al Harthi, A.; Al Hajri, A.; Coy, G.A.; Al Salmi, W.; Al Rawahi, Z. The Sudair Formation: From Seal to Reservoir, Oman. In Proceedings of the ADIPEC, Abu Dhabi, United Arab Emirates, 3–6 November 2025.
108. Matthieu, D.; Pierre, B.; Fatimah, A.; Feng, L. Sedimentology, sequence stratigraphy, palynology and diagenetic evaluation of the Triassic Jilh Formation. New insights from Saudi Arabia. *J. Afr. Earth Sci.* **2022**, *196*, 104714. [CrossRef]
109. Benoît, I.; Yves-Michel, M.; Abdullah, M.; Saleh, D.; Sophie, V. Managing clastic reservoir heterogeneity I: Sedimentology and sequence stratigraphy of the Late Triassic Minjur Sandstone at the Khashm al Khalta type locality, Central Saudi Arabia. *GeoArabia* **2012**, *17*, 17–56. [CrossRef]
110. Abdullatif, O. Insights on spatial variography and outcrop-subsurface relationship of sandstone reservoir properties: A case study from the Late Triassic Minjur Formation, central Saudi Arabia. *J. Afr. Earth Sci.* **2019**, *153*, 173–184. [CrossRef]
111. Wolpert, P.; Bartenbach, M.; Suess, P.; Rausch, R.; Aigner, T.; Le Nindre, Y. Facies analysis and sequence stratigraphy of the uppermost Jurassic– Lower Cretaceous Sulaiy Formation in outcrops of central Saudi Arabia. *GeoArabia* **2015**, *20*, 67–122. [CrossRef]
112. Eckhardt, K. A comparison of baseflow indices, which were calculated with seven different baseflow separation methods. *J. Hydrol.* **2008**, *352*, 168–173. [CrossRef]
113. Moon, S.K.; Woo, N.C.; Lee, K.S. Statistical analysis of hydrographs and water-table fluctuation to estimate groundwater recharge. *J. Hydrol.* **2004**, *292*, 198–209. [CrossRef]
114. Cheng-Haw; Lee; Chen, W.-P.; Lee, R.-H. Estimation of groundwater recharge using water balance coupled with base-flow-record estimation and stable-base-flow analysis. *Environ. Geol.* **2006**, *51*, 73–82. [CrossRef]
115. Kannan, P.; Balasubramaniyan, G.; Mani, S.; Swaminathan, B.; Murugesan, B. Hydrogeochemical assessment and suitability evaluation of groundwater in a hard rock region: A case study of Jambuduraikottai, Tamil Nadu. *DYSONA-Appl. Sci.* **2026**, *7*, 142–151. [CrossRef]
116. Atalla, M.A.; Shebl, A.; Đurin, B.; Kranjčić, N.; AlMetwaly, W.M. Assessment of Groundwater Potential Zones in Kuwait's Semi-Arid Region: A Hybrid Approach of Multi-Criteria Decision Making, Google Earth Engine, and Geospatial Techniques. *Sci. Rep.* **2024**, *14*, 29938. [CrossRef] [PubMed]
117. Taylor, E.M.; Malhotra, J.K.; Mehta, M.L. *An Investigation of the Rise of Water Table in the Upper Chenab Canal Area*; Punjab Irrigation Research Institute: Lahore, Pakistan, 1933; p. 187.
118. Wilsdon, B.H.; Sarathy, P. *A Statistical Examination of the Sensitivity of a Water Table to Rainfall and Irrigation*; Irrigation Research Institute: Lahore, Pakistan, 1931.
119. Singh, G.D.S. Groundwater resources of doon valley, India. In Proceedings of the International Symposium on Development of Groundwater Resources, Madras, India, 26–29 November 1973; pp. 109–121. [CrossRef]
120. Rangarajan, R.; Athavale, R.N. Annual replenishable ground water potential of India-an estimate based on injected tritium studies. *J. Hydrol.* **2000**, *234*, 38–53. [CrossRef]
121. Chandra, S.; Saxena, R.S. Water balance study for estimation of groundwater resources. *Irrig. Power J.* **1975**, *32*, 443–449.

122. Tonder, G.V.; Kirchner, J. Estimation of natural groundwater recharge in the Karoo aquifers of South Africa. *J. Hydrol.* **1990**, *121*, 395–419. [CrossRef]
123. Wilson, E.M. *Engineering Hydrology: Solutions to Problems*, 4th ed.; Macmillan: Basingstoke, UK, 1990.

Disclaimer/Publisher's Note: The statements, opinions and data contained in all publications are solely those of the individual author(s) and contributor(s) and not of MDPI and/or the editor(s). MDPI and/or the editor(s) disclaim responsibility for any injury to people or property resulting from any ideas, methods, instructions or products referred to in the content.